

12-14-2013

Modeling Dendritic Solidification using Lattice Boltzmann and Cellular Automaton Methods

Mohsen Eshraghi Kakhki

Follow this and additional works at: <https://scholarsjunction.msstate.edu/td>

Recommended Citation

Eshraghi Kakhki, Mohsen, "Modeling Dendritic Solidification using Lattice Boltzmann and Cellular Automaton Methods" (2013). *Theses and Dissertations*. 3140.
<https://scholarsjunction.msstate.edu/td/3140>

This Dissertation - Open Access is brought to you for free and open access by the Theses and Dissertations at Scholars Junction. It has been accepted for inclusion in Theses and Dissertations by an authorized administrator of Scholars Junction. For more information, please contact scholcomm@msstate.libanswers.com.

Modeling dendritic solidification using lattice Boltzmann and cellular automaton
methods

By

Mohsen Eshraghi Kakhki

A Dissertation
Submitted to the Faculty of
Mississippi State University
in Partial Fulfillment of the Requirements
for the Degree of Doctor of Philosophy
in Mechanical Engineering
in the Department of Mechanical Engineering

Mississippi State, Mississippi

December 2013

Copyright by
Mohsen Eshraghi Kakhki
2013

Modeling dendritic solidification using lattice Boltzmann and cellular automaton
methods

By

Mohsen Eshraghi Kakhki

Approved:

Sergio D. Felicelli
(Director of Dissertation)

Mark F. Horstemeyer
(Committee Member)

Rogelio Luck
(Committee Member)

Mohsen Asle Zaeem
(Committee Member)

Kalyan K. Srinivasan
(Graduate Coordinator)

Royce O. Bowden
Interim Dean
Bagley College of Engineering

Name: Mohsen Eshraghi Kakhki

Date of Degree: December 14, 2013

Institution: Mississippi State University

Major Field: Mechanical Engineering

Major Professor: Sergio D. Felicelli

Title of Study: Modeling dendritic solidification using lattice Boltzmann and cellular automaton methods

Pages in Study: 103

Candidate for Degree of Doctor of Philosophy

This dissertation presents the development of numerical models based on lattice Boltzmann (LB) and cellular automaton (CA) methods for solving phase change and microstructural evolution problems. First, a new variation of the LB method is discussed for solving the heat conduction problem with phase change. In contrast to previous explicit algorithms, the latent heat source term is treated implicitly in the energy equation, avoiding iteration steps and improving the formulation stability and efficiency. The results showed that the model can deal with phase change problems more accurately and efficiently than explicit LB models.

Furthermore, a new numerical technique is introduced for simulating dendrite growth in three dimensions. The LB method is used to calculate the transport phenomena and the CA is employed to capture the solid/liquid interface. It is assumed that the dendritic growth is driven by the difference between the local actual and local equilibrium composition of the liquid in the interface. The evolution of a three-dimensional (3D) dendrite is discussed. In addition, the effect of undercooling and degree of anisotropy on the kinetics of dendrite growth is studied.

Moreover, effect of melt convection on dendritic solidification is investigated using 3D simulations. It is shown that convection can change the kinetics of growth by affecting the solute distribution around the dendrite. The growth features of two-dimensional (2D) and 3D dendrites are compared. Furthermore, the change in growth kinetics and morphology of Al-Cu dendrites is studied by altering melt undercooling, alloy composition and inlet flow velocity.

The local-type nature of LB and CA methods enables efficient scaling of the model in petaflops supercomputers, allowing the simulation of large domains in 3D. The model capabilities with large scale simulations of dendritic solidification are discussed and the parallel performance of the algorithm is assessed. Excellent strong scaling up to thousands of computing cores is obtained across the nodes of a computer cluster, along with near-perfect weak scaling. Considering the advantages offered by the presented model, it can be used as a new tool for simulating 3D dendritic solidification under convection.

DEDICATION

To my parents, for their unconditional love, support, and patience.

ACKNOWLEDGEMENTS

First of all, I would like to express my deepest gratitude to my major advisor, Dr. Sergio D. Felicelli, whose great mentorship, assistance, friendship, and trust made this possible. Dr. Felicelli was not only a mentor, but a friend who taught me a lot, not only about science and engineering, but also about life. Also, I would like to thank my family for their continuous support and encouragement in every stage of my life. Moreover, I would like to appreciate Dr. Horstemeyer, Dr. Luck, and Dr. Asle Zaeem for taking the time to review this work. My special thanks to Dr. Bohumir Jelinek for his wonderful assistance and support during the course of this work, particularly for his important contribution to the results presented in Chapter V. I gratefully acknowledge the collaboration of Mr. Daniel Johnson with the validation of the fluid flow model.

This work was funded by the National Science Foundation through Grant Number CBET-0931801. In addition, I would like to acknowledge the Center for Advanced Vehicular Systems (CAVS) in Mississippi State University for their sponsorship and the Extreme Science and Engineering Discovery Environment (XSEDE) for providing the computational resources.

TABLE OF CONTENTS

DEDICATION	ii
ACKNOWLEDGEMENTS	iii
LIST OF TABLES	vii
LIST OF FIGURES	viii
CHAPTER	
I. INTRODUCTION	1
1.1 Research background	1
1.2 Research objectives	4
1.3 Intellectual merit	5
1.4 Broader impact	5
1.5 Dissertation structure	6
1.6 References	7
II. AN IMPLICIT LATTICE BOLTZMANN MODEL FOR HEAT CONDUCTION WITH PHASE CHANGE	10
2.1 Introduction	10
2.2 Numerical formulation	11
2.2.1 Continuum formulation	11
2.2.2 Lattice Boltzmann model	12
2.2.2.2 LBM boundary conditions	16
2.2.2.2.1 Dirichlet boundary conditions	17
2.2.2.2.2 Neumann boundary condition	17
2.2.2.3 Numerical procedure	18
2.3 Verification and discussion	19
2.3.1 One-dimensional melting of a pure metal	19
2.3.2 One-dimensional solidification of a binary alloy	24
2.3.3 Two-dimensional solidification of a binary alloy	28
2.3.4 Comparison of computational performance in LBM and FEM	33
2.4 Conclusions	35
2.5 References	37

III.	THREE DIMENSIONAL SIMULATION OF SOLUTE-DRIVEN DENDRITE GROWTH USING LATTICE BOLTZMANN AND CELLULAR AUTOMATON METHODS.....	39
3.1	Introduction.....	39
3.2	Model description	40
3.3	Results and discussion	44
3.3.1	Growth kinetics.....	44
3.3.2	Model validation	45
3.3.3	Solute distribution.....	48
3.3.4	Effect of anisotropy of the surface energy	49
3.4	Conclusions.....	51
3.5	References.....	53
IV.	THREE-DIMENSIONAL LATTICE BOLTZMANN MODELING OF DENDRITIC SOLIDIFICATION UNDER FORCED CONVECTION.....	55
4.1	Introduction.....	55
4.2	Model description	56
4.3	Results and discussion	60
4.3.1	Validation.....	60
4.3.1.1	Fluid flow.....	60
4.3.1.2	Solute transport	62
4.3.2	Dendrite growth under melt convection	64
4.3.2.1	Kinetics of growth under forced convection.....	64
4.3.2.2	Comparison of 2D and 3D simulations.....	68
4.3.2.3	Effect of melt undercooling	71
4.3.2.4	Effect of inlet velocity	73
4.3.2.5	Effect of alloy composition.....	75
4.4	Conclusions.....	78
4.5	References.....	80
V.	LARGE-SCALE SIMULATION OF DENDRITIC SOLIDIFICATION.....	82
5.1	Introduction.....	82
5.2	Parallelization	82
5.3	Parallel performance	85
5.3.1	Strong scaling.....	85
5.3.2	Weak scaling.....	86
5.4	Large scale columnar growth.....	87
5.5	Large scale columnar growth under forced convection.....	93
5.6	Conclusions.....	94
5.7	References.....	95

VI.	SUMMARY AND FUTURE WORKS	96
6.1	Summary	96
6.2	Awards and recognition	98
6.3	Future works	99
6.3.1	Employ the presented model to simulate various casting and solidification processes	99
6.3.2	Simulation of freckle formation during alloy solidification	100
6.3.3	Calculation of the interdendritic permeability	101
6.3.4	A pure lattice Boltzmann model for dendrite growth	101
6.3.5	A multi-grid lattice Boltzmann model with superior computational performance	102
6.4	References	103

LIST OF TABLES

2.1	Thermo-physical properties of the studied materials.....	20
3.1	Physical properties of Al-Cu alloy used in the simulations.....	43
3.2	Comparison of dendrite tip velocities for Al-4wt%Cu alloy obtained from present LB-CA , LGK ($\sigma^*=0.05$), CA and PF models.....	48
4.1	Fluid characteristic quantities for steady state laminar flow over a cylinder. Simulation results are listed for three different node spacings. Lower and upper bounds present the estimated interval for the exact results [8].	62

LIST OF FIGURES

2.1	Schematic diagram showing D2Q9 lattice and the unknown distribution functions at west wall and northwest corner.	13
2.2	Schematic of the one-dimensional melting of the pure material showing coordinates, initial and boundary conditions, liquid and solid zones, and the interface position.	20
2.3	Comparison between LBM and analytical thermal histories of the points located at 1, 5, 10, and 20 mm from the hot wall for the one-dimensional pure metal melting problem.	22
2.4	Comparison between LBM and analytical solutions for temperature profiles after 1, 5, 20, and 60 seconds for the one-dimensional pure metal melting problem.	23
2.5	LBM and analytical solutions of the interfacial position for the one-dimensional pure metal melting problem.	24
2.6	Schematic of the one-dimensional solidification of an Al-3%Cu alloy showing coordinates, initial and boundary conditions, liquid, solid and mushy zones, and the interfacial positions.	25
2.7	Comparison between LBM and FEM cooling curves of the points located at 1, 10, and 25 millimeters from the cold wall for the one-dimensional binary alloy solidification problem.	26
2.8	Comparison between LBM and FEM solutions for temperature profiles after 1, 5, 20, and 60 seconds for the one-dimensional binary alloy solidification problem.	27
2.9	LBM and FEM solutions of the liquid/mushy zone (L/M) and mushy zone/solid (M/S) interfacial positions for the one-dimensional binary alloy solidification problem.	28
2.10	Schematic of the two-dimensional solidification of the Al-3%Cu binary alloy showing coordinates, dimensions, initial and boundary conditions.	29

2.11	Comparison between LBM and FEM cooling curve of the point located at the center of the model for the two-dimensional binary alloy solidification problem.	30
2.12	Comparison between LBM and FEM temperature profiles after 15, 45, 90, 120 seconds for the two-dimensional solidification problem.	31
2.13	Color contours comparing LBM and FEM temperature distributions at different times for the two-dimensional solidification problem.	32
2.14	Color contours comparing LBM and FEM solid percentages at different times for the two-dimensional solidification problem.	33
2.15	Running time of LBM and FEM models for different domain sizes.	34
3.1	D3Q15 lattice.	41
3.2	Simulated dendrite morphologies for $\Delta T=4.5$ °C and $\varepsilon=0.04$. From left to right, after 3, 7, 10, and 15 ms.	44
3.3	Comparison of the dendritic features simulated by the present model with the theoretical values over a range of undercoolings: (a) tip velocity, (b) tip radius, (c) Peclet number, and (d) σ^*	45
3.4	Solute concentration field around the dendrite for $\Delta T=4.5$ °C and $\varepsilon=0.04$ after 15 ms.	49
3.5	Variation of dendrite morphology and tip velocity with respect to anisotropy parameter.	51
4.1	Schematic illustration of the simulation domain.	60
4.2	Configuration and boundary conditions for the benchmark problem of steady state laminar flow over a cylinder [8].	62
4.3	Comparison between the solute distribution calculated using LB and analytical models for diffusion-advection under $U_0=10$ mm/s after 2 ms.	63
4.4	Evolution of dendritic structures under melt convection after (a) 2, (b) 4, (c) 6, and (d) 8 ms.	66
4.5	2D sections showing the morphological changes of the 3D dendrite growing under melt convection.	67
4.6	Snapshot of a 3D solutal dendrite growing under melt convection.	68
4.7	Solute distribution around 2D and 3D dendrites.	70

4.8	Contours showing the x-component of velocity around 2D and 3D dendrites.	70
4.9	Variation of average tip velocity with undercooling for upstream, downstream, and transverse branches of a dendrite growing under inlet velocity of $U_0=7$ mm/s and the case without melt convection.	72
4.10	Comparison of dendritic morphologies growing in melts with different degrees of undercooling: top: $\Delta T=4$ °C, and bottom: $\Delta T=3$ °C.	73
4.11	Variation of average tip velocity with inlet melt velocity for Al-3wt%Cu alloy with $\Delta T=4.5$ °C.	74
4.12	Effect of inlet velocity on the morphology of Al-3wt%Cu dendrites. Different colors represent different inlet velocities: 0, 4, and 8 mm/s.	75
4.13	Variation of average tip velocity with initial alloy composition under $U_0=7$ mm/s, and $\Delta T=4.5$ °C.	77
4.14	Effect of alloy composition on the dendritic morphology under inlet velocity of $U_0=7$ mm/s, and $\Delta T=4.5$ °C.	77
5.1	Populating the ghost values (green area in part (a)) on the execution core 5 Each subdomain permanently stores an extra “ghost” layer of values to be received from (or to be sent to) the neighboring subdomains. Synchronously with receiving the data, the execution core 5 sends the data in the direction opposite to where the data is received from.	84
5.2	Speed up performance (increasing number of processors with a fixed domain size).	87
5.3	Scale up performance (fixed processor load by scaling the domain size). The calculation time at each point is relative to the calculation time when the smallest number of cores was deployed.	88
5.4	Columnar dendrites growing in an undercooled melt of the Al-3wt.%Cu alloy.	89
5.5	Solute distribution around 3D columnar dendrites.	90
5.6	Large scale simulation of 3D columnar dendrite growth in a 1 mm^3 domain with around 36 billion grid points and 4000 initial seeds.	92
5.7	3D columnar dendrites growing in an undercooled melt of Al-3wt%Cu. The domain contains around 173 million 3D lattice points that corresponds to a $180\times 180\times 144\text{ (}\mu\text{m)}^3$ physical domain.	93

CHAPTER I

INTRODUCTION

1.1 Research background

Dendrites are common microstructures observed in most crystalline materials, especially metallic alloys. Studying the solidification process and investigating the kinetics of dendrite growth is of utmost importance, as the characteristics of the dendrites strongly affect the properties of metallic alloys.

Numerical models have been undertaken by several researchers to simulate the microstructural evolution during solidification of alloys. The majority of models of dendritic growth at the microscopic scale can be categorized into three main types: those based on the Phase-Field (PF) method [1–5]; models based on the Level Set (LS) method [6–9], and models that perform a Direct Interface Tracking (DIT) [10–13]. Of these methods, the PF is probably the most powerful, because it can deal directly with any morphological complexity by introducing a field variable that eliminates the need to explicitly find the interface. However, it is very computationally taxing even when combined with adaptive meshing methods. The LS method also interchanges the interface with a field variable (the level set), but requires knowledge of the direction in which the solid front is advancing, its velocity, and the calculation of the vector normal to the interface; which makes it less effective than the PF method in complex three-dimensional geometries. DIT is the simplest and computationally the most efficient of the methods,

but it is also less powerful because it requires the calculation of the temperature gradients at the interface in addition to the normal velocity and curvature of the interface.

Moreover, the complexity for handling interfaces in all possible solidification conditions limits the applicability of DIT methods.

Despite the extensive work that has been done in two dimensions, fewer three-dimensional calculations of dendritic solidification at the microscale have been reported [14–23]. Some of these works include convection effects, but only few recent publications [14, 19, 20, 23] consider binary alloys. Regardless of the method of choice, the computational effort is significantly larger than in two-dimensions, this is due in part to the fact that the growth velocities are higher in three-dimensions, and also to the presence of the capillary length scale, that cannot be fully resolved.

For the reasons explained above, it is apparent that the above-mentioned methods are not very well suited for three-dimensional calculations of dendritic growth. On the other hand, methods based on the Cellular Automaton (CA) have been extensively developed and offer an alternative [24–32] with the potential to allow for reasonably accurate calculations in bigger domains. These techniques do not capture the same level of detail at the solid-liquid interface as methods based on PF or DIT. In particular, initial CA models could not account for the effect of undercooling on the growth velocity except ahead of the dendrite tips. However, in recent years they have been combined with finite element and/or finite difference/volume solutions of the energy and solute transport equations and developed to a point where solute concentration, undercooling, and latent heat dissipation can be properly modeled [28, 29]; crystal anisotropy effects have also been incorporated.

Cellular automata (CA) models are often characterized as being simple in their construction and yet able to produce very complicated behavior. This property of CA models has been exploited to produce computer simulations of various aspects of microstructural evolution occurring during solidification.

One of the most elaborate early CA models for calculation of grain growth, combining stochastic nucleation, diffusional growth and macroscopic heat conduction was proposed by Gandin and Rappaz [24, 25] as an extension to the stand-alone CA model. Sanchez and Stefanescu [27] and Zhu and Stefanescu [31] proposed a model based on the cellular automaton technique for the simulation of dendritic growth controlled by solutal effects in the low Peclet number regime. One of the innovative aspects of this model is that it does not use an analytical solution to determine the velocity of the solid-liquid interface as is common in other models.

The Lattice Boltzmann method (LBM) is a relatively new Computational Fluid Dynamics (CFD) technique for solving flow and thermal problems. While the traditional numerical methods are based on the discretization of conservation equations of continuum mechanics, LBM relies on the solution of a minimal form of Boltzmann kinetic equation for a group of fictive particles in a discretized domain. The fictive particles stream across the lattice along the links connecting neighboring lattice sites, and then undergo collisions upon arrival at a lattice site. For simulating physical phenomena, the collisions among particles must obey suitable physical laws. The fundamental idea of the LBM is to construct kinetic models that incorporate the physics of microscopic processes so that the macroscopic averaged properties obey the desired laws. More

details about the LB method can be found in the reference books published on LBM [33-36].

LBM is an excellent tool for simulation of mass and energy transport phenomena. Since the 1990s, LBM has been utilized for solving a wide variety of transport problems in science and engineering. The major advantages of LBM in comparison with traditional CFD methods consist of simple implementation, capability for simulating highly complex geometries and boundaries, computational efficiency and inherent parallel-processing structure. Considering these special capabilities, LBM has attracted the attention of many researchers and scientists.

1.2 Research objectives

The final objective of this work is to develop a parallel three-dimensional lattice-Boltzmann model to simulate dendritic growth during alloy solidification under melt convection in macro-scale domains. An innovating aspect of this research is that the simulations will be done in a macroscopic domain, but with microscale resolution. As such, the computations will involve calculating fluid flow and solute transport in an evolving and highly irregular microstructure which may include hundreds or thousands of dendrites. In order to address the high computational demand expected in these simulations, a new numerical methodology based on the combination of the CA and the LB methods will be developed.

The combined CA-LB technique allows the simulation of the solidification microstructure in a small macro-domain with modest computer resources. However, the development of the CA-LB technique would open the way for the direct numerical simulation of solidification microstructures in large macro-domains when the technique is

implemented in the coming generation of massively parallel supercomputers. It is important to emphasize that the proposed research is on fundamental solidification science and hence relevant to a wide spectrum of applications.

1.3 Intellectual merit

The outcome of this research is a first-time tool to numerically simulate the growth of a dendritic structure in a macroscale domain under the effect of strong fluid flow. The correct determination of the solidification microstructure is of critical importance to understand the subsequent solid phase transformations during cooling. The knowledge developed in this work advances the state of understanding of solidification phenomena in the microscale and contributes to improved numerical predictions of the solidification microstructure. The large computational requirements of the calculations expand the capabilities of cellular automata, lattice Boltzmann models, and parallelization algorithms, contributing to the advance and wider acceptance of these techniques.

1.4 Broader impact

The findings of this research directly impact the solidification research community, software developers and several technologies involving solidification processing. Currently, all major commercial codes simulating alloy solidification rely on continuum-type mushy zone models developed in the 80's that use unrealistic microstructure approximations based on empirical correlations of permeability. The incorporation of new numerical developments is needed for more reliable predictions of defects during solidification. This research makes a significant contribution to this end.

1.5 Dissertation structure

Chapter I presents a literature review and describes the motivation of this work.

Chapter II discusses the development of a new variation of the LB method for solving the heat conduction problem with phase change.

Chapter III describes a three-dimensional LB-CA model for solute-driven dendrite growth.

Chapter IV explains three-dimensional simulation of dendrite growth under forced convection. The influence of different parameters on the dendritic morphologies and growth kinetics are discussed.

Chapter V presents large scale simulations of dendrite growth and discusses the parallel performance of the model.

Chapter VI contains a summary of the work and the recommendations for future research works in this area.

1.6 References

- [1] W. J. Boettinger, J. A. Warren, C. Beckermann, A. Karma, Phase-field simulations of solidification, *Annual Review of Materials Research* 32 (2002) 132-194.
- [2] A. Badillo, Beckermann C, Phase-field simulation of the columnar-to-equiaxed transition in alloy solidification, *Acta Materialia* 54 (2006) 2015-2026.
- [3] J. J. Hoyt, M. Asta, A. Karma, Atomistic and continuum modeling of dendritic solidification, *Materials Science and Engineering R* 41 (2003) 121-163.
- [4] A. Karma, W. J. Rappel, Quantitative phase-field modeling of dendritic growth in two and three dimensions, *Physical Review E* 57 (1998) 4323-4349.
- [5] N. Provatas, N. Goldenfeld, J. A. Dantzig, Adaptive mesh refinement computation of solidification microstructures using dynamic data structures, *Journal of Computational Physics* 148 (1999) 265-290.
- [6] F. Gibou, R. P. Fedkiw, L-T. Cheng , M. Kang, A second-order-accurate symmetric discretization of the Poisson equation in irregular domains, *Journal of Computational Physics* 176 (2002) 205-227.
- [7] F. Gibou, R. Fedkiw, R. Caflisch, S. Osher, A level set approach for the numerical simulation of dendritic growth, *Journal of Scientific Computing* 19 (2003) 183-199.
- [8] Y-T. Kim, N. Goldenfeld, J. A. Dantzig, Computation of dendritic microstructures using a level set method, *Physical Review E* 62 (2000) 2471-2474.
- [9] S. Osher, R. P. Fedkiw, Level set methods: an overview and some recent results, *Journal of Computational Physics* 169 (2001) 463-502.
- [10] R. Merle, J. Dolbow, Solving thermal and phase change problems with extended finite element method, *Computational Mechanics* 28 (2002) 339-350.
- [11] A. Schmidt, Approximation of crystalline dendritic growth in two space dimensions, *Acta Mathematica Universitatis Comenianae* 67 (1998) 57-68.
- [12] H. S. Udaykumar, R. Mittal, W. Shyy, Computation of solid-liquid phase fronts in the sharp interface limit on fixed grids, *Journal of Computational Physics* 153 (1999) 535-574.
- [13] P. Zhao, J. C. Heinrich, Front-tracking finite element method for dendritic solidification, *Journal of Computational Physics* 173 (2001) 765-796.

- [14] J-H. Jeong, N. Goldenfeld, J. A. Dantzig, Phase field model for three-dimensional dendritic growth with fluid flow, *Physical Review E* 65 (2001) 041602.
- [15] J-H. Jeong, J. A. Dantzig, N. Goldenfeld, Dendritic growth with a fluid flow in pure materials, *Metallurgical and Materials Transactions A* 34 (2003) 459-466.
- [16] A. Karma, W. J. Rappel, Phase-field simulation of three-dimensional dendrites: is solvability theory correct?, *Journal of Crystal Growth* 174 (1997) 54-64.
- [17] R. Kobayashi, A numerical approach to three-dimensional dendritic solidification, *Experimental Mathematics* 3 (1994) 59-8.
- [18] Y. Lu, C. Beckermann, A. Karma, Convective effects in three-dimensional dendritic. *Materials Research Society Symposium Proceedings* 701 (2002) T2.2.1-10.
- [19] Y. Lu, C. Beckermann, J. C. Ramirez, Three-dimensional phase-field simulations of the effect of convection on free dendritic growth, *Journal of Crystal Growth* 280 (2005) 320-334.
- [20] J. Narski, M. Picasso, Adaptive 3-D finite elements with high aspect ratio for dendritic growth of a binary alloy including fluid flow induced by shrinkage, *Fluid Dynamics & Materials Processing* 1 (2006) 1-13.
- [21] A. Schmidt, Computation of three dimensional dendrites with finite elements, *Journal of Computational Physics* 125 (1996) 293-312.
- [22] P. Zhao, J. C. Heinrich, D. R. Poirier, Numerical simulation of crystal growth in three dimensions using a sharp-interface finite element method, *International Journal for Numerical Methods in Engineering* 71 (2007) 25-46.
- [23] L. Yuan, P. D. Lee, Numerical Simulations on Dendritic Solidification under Forced and Natural Convection for Binary Alloys: 2D vs. 3D, *Modelling and Simulation in Materials Science and Engineering* 18 (2010) 055008.
- [24] C. A. Gandin, M. Rappaz, A coupled finite element-cellular automaton model for the prediction of dendritic grain structures in solidification processes, *Acta Metallurgica et Materialia* 42 (1994) 2233-2246.
- [25] C. A. Gandin, M. Rappaz, 3D Cellular automaton algorithm for the prediction of dendritic grain growth, *Acta Materialia* 45 (1997) 2187-2195.
- [26] S. G. R. Brown, N. B. Bruce, 3-dimensional cellular-automaton models of microstructural evolution during solidification, *Journal of Materials Science* 30 (1995) 1144-1150.

- [27] L. B. Sanchez, D. M. Stefanescu, growth of solutal dendrites: a cellular automaton model and its quantitative capabilities, *Metallurgical and Materials Transactions A* 34 (2003) 367-382.
- [28] G. Guillemot, C. A. Gandin, H. Combeau, R. Heringer, A new cellular automaton-finite element coupling scheme for alloy solidification, *Modelling and Simulation in Materials Science and Engineering* 12 (2004) 545-556.
- [29] W. Wang, P. D. Lee, M. McLean, A model of solidification microstructures in nickel-based superalloys: predicting primary dendrite spacing selection, *Acta Materialia* 51 (2003) 2971-2987.
- [30] M. F. Zhu, C. P. Hong, A three dimensional modified cellular automaton model for the prediction of solidification microstructures, *ISIJ International*, 42 (2002) 520-526.
- [31] M. F. Zhu, D. M. Stefanescu, Virtual front tracking model for the quantitative modeling of dendritic growth in solidification of alloys, *Acta Materialia* 55 (2007) 1741-1755
- [32] M. F. Zhu, S. Y. Lee, C. P. Hong, Modified cellular automaton model for the prediction of dendritic growth with melt convection, *Physical Review E* 69 (2004) 061610.
- [33] D. Wolf-Gladrow, *Lattice-gas cellular automata and lattice Boltzmann models: an introduction*, Springer-Verlag, Berlin-Heidelberg (2000).
- [34] S. Succi, *The lattice Boltzmann equation for fluid dynamics and beyond, numerical mathematics and scientific computation*, Oxford University Press (2001).
- [35] M. C. Sukop, D. T. Thorne, *Lattice Boltzmann modeling; an introduction for geoscientists and engineers*, Springer-Verlag, Berlin-Heidelberg (2006).
- [36] A. Mohamad, *Lattice Boltzmann method fundamentals and engineering applications with computer codes*, Springer, London (2011).

CHAPTER II

AN IMPLICIT LATTICE BOLTZMANN MODEL FOR HEAT CONDUCTION WITH PHASE CHANGE

2.1 Introduction

During the recent years the application of LBM has been extended to many areas of fluid and thermal sciences. Heat conduction with phase change is one of the challenging problems that has many applications in various fields of science and engineering, particularly in metallurgical processes associated with phase change like casting, solidification, solid-state phase transformations and many other material processes.

Wolf-Gladrow [1] was one of the first to develop an LB formulation for diffusion. De Fabritiis *et al.* [2] developed a thermal model for solid-liquid phase change problems by considering different particles for solid and liquid phases. van der Sman *et al.* [3] developed a one-dimensional LB model for simulation of heat and mass transport in packed cut flowers. Miller *et al.* [4] developed a lattice Boltzmann model for anisotropic crystal growth from melt with enhanced computational capabilities. They used similar particles for different phases along with a phase field scheme. Semma *et al.* [5] adopted LBM to solve melting and solidification problems. They used two distribution functions for fluid flow and heat transfer simulations. The phase interface was traced by using partial or probabilistic bounce back approach. Jiaung *et al.* [6] were the first researchers who

introduced an extended lattice Boltzmann equation governed by the heat conduction equation in conjunction with enthalpy method. Chatterjee and Chakraborty [7-9] and Chatterjee [10, 11] published a series of papers on modeling solid-liquid phase transition problems using LBM with enthalpy approach. It should be noted that explicit approaches have been used in all studies that employed the enthalpy formulation for phase change calculations [6-11], in which iterations are needed in order to deal with the latent heat source term.

In this chapter, an alternative approach of simulation of heat conduction problem with phase change by using the lattice Boltzmann method is introduced. While an explicit approach was used in previous studies, a novel implicit formulation was adopted for the latent heat source term. The Bhatnagar-Gross-Krook (BGK) [12] approximation with a D2Q9 lattice was applied and different boundary conditions including Dirichlet and Neumann boundary conditions were tested. The developed model was utilized to simulate the heat conduction during phase change in materials with constant transition temperature and materials with transition temperature range. The obtained results were compared with the results of analytical solutions and other numerical models and good consistency was observed.

2.2 Numerical formulation

2.2.1 Continuum formulation

The Fourier heat conduction equation with phase change can be written as

$$\frac{\partial}{\partial t}(\rho C_p T) = \nabla \cdot (k \nabla T) + \frac{\partial}{\partial t}(\rho \Delta H) \quad (2.1)$$

where ρ , C_p , and k are density, specific heat, and heat conductivity, respectively.

ΔH is the amount of heat released due to phase change.

For constant thermo-physical properties, the equation can be simplified to

$$\frac{\partial T}{\partial t} = \alpha \nabla^2 T - \Phi \quad (2.2)$$

where α is the heat diffusivity and Φ is a source term calculated as

$$\Phi = \frac{\partial f_l}{\partial t} \frac{L}{c_p} \quad (2.3)$$

where L is the phase change latent heat and f_l is the volume fraction of liquid.

2.2.2 Lattice Boltzmann model

Lattice Boltzmann models are simpler than the original Boltzmann equation. The domain is discretized into a number of pseudo particles located on the nodes of the lattice and time is discretized into some distinct steps. There are a few possibilities for spatial position of the particles. One of the most well-known LBM lattices is D2Q9 which has two dimensions and nine velocities. Figure 2.1 shows the D2Q9 lattice structure which is used in this study. The discrete velocities of D2Q9 lattice in 2D Cartesian direction are determined as

$$e_i = \begin{cases} (0,0) & i = 0 \\ (\cos[(i-1)\pi/2], \sin[(i-1)\pi/2])c & i = 1-4 \\ (\cos[(2i-9)\pi/4], \sin[(2i-9)\pi/4])\sqrt{2}c & i = 5-8 \end{cases} \quad (2.4)$$

where $c = \Delta x / \Delta t$ is lattice speed, Δx is lattice spacing and Δt is time step.

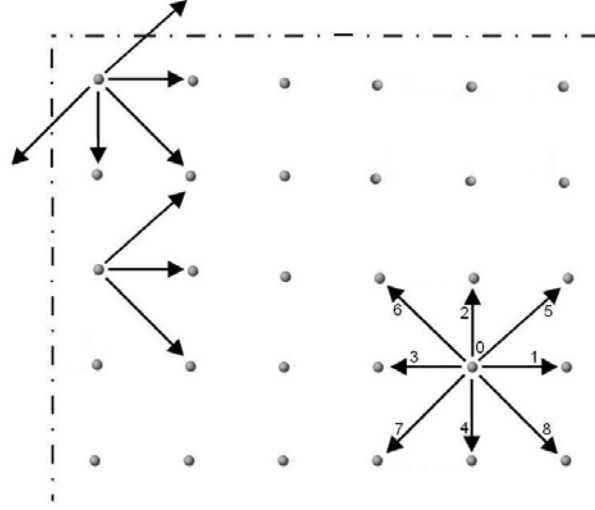


Figure 2.1 Schematic diagram showing D2Q9 lattice and the unknown distribution functions at west wall and northwest corner.

The distribution function, $g_i(x, t)$, is defined as the probability of finding a particle moving in direction i . Then, the macroscopic temperature, $T(x, t)$, can be calculated as

$$T(x, t) = \sum_{i=0}^8 g_i(x, t) \quad (2.5)$$

The kinetic equation for the distribution functions without an external source term can be written as

$$\partial_t g_i(x, t) + e_i \cdot \nabla g_i(x, t) = \Omega_i(g) \quad (2.6)$$

where e_i is the velocity in direction i and $\Omega_i(g)$ represents the rate of local change in the distribution function due to collisions. According to BGK (Bhatnagar-Gross-Krook) approximation, this term can be expressed as

$$\Omega_i(g) = -\omega[g_i(x, t) - g_i^{eq}(x, t)] \quad (2.7)$$

where ω is a relaxation parameter and $g_i^{eq}(x, t)$ is the equilibrium distribution function which can be described as

$$g_i^{eq}(x, t) = w_i T(x, t) \quad (2.8)$$

where w_i is the weight factor in direction i and for different directions of the D2Q9 lattice is given as follows

$$w_i = \begin{cases} 4/9 & i = 0 \\ 1/9 & i = 1 - 4 \\ 1/36 & i = 5 - 8 \end{cases} \quad (2.9)$$

After discretization, the Equation (2.6) can be summarized as

$$g_i(x + e_i \Delta t, t + \Delta t) - g_i(x, t) = -\omega \Delta t (g_i(x, t) - g_i^{eq}(x, t)) \quad (2.10)$$

where the LHS can be considered as streaming term and the RHS can be considered as collision term. Collision in LBM terminology means relaxation towards the equilibrium. The collision term for a specific particle can be written as

$$g_i(x, t + \Delta t) = (1 - \omega \Delta t) g_i(x, t) + \omega \Delta t g_i^{eq}(x, t) \quad (2.11)$$

By analogy with the continuum formulation, a source term can be added to the equation

$$g_i(x, t + \Delta t) - g_i(x, t) = -\omega \Delta t (g_i(x, t) - g_i^{eq}(x, t)) - \Delta t w_i \Phi \quad (2.12)$$

It is proved that the Equation (2.12) can reproduce the continuum Equation (2.2) using the Chapman-Enskog expansion. For this to be true, the thermal diffusivity, α , in the D2Q9 lattice should be set as follows [6]

$$\alpha = \frac{c^2 \Delta t}{6} \left(\frac{2}{\omega} - 1 \right) \quad (2.13)$$

In the discretized form, Φ is defined by the following equation

$$\Phi = \frac{L}{c_p} \frac{\Delta f_l}{\Delta t} \quad (2.14)$$

where Δf_l is the change in volume fraction of liquid during the time step Δt . The volume fraction of liquid is calculated with the lever rule formula:

$$f_l = \frac{T - T_s}{T_l - T_s} \quad (2.15)$$

where T_l and T_s are liquidus and solidus temperatures respectively. Considering the Equation (2.5), the change in the volume fraction of liquid, Δf_l , can be written as

$$\begin{aligned} \Delta f_l &= f_l(x, t + \Delta t) - f_l(x, t) = \frac{T(x, t + \Delta t) - T_s}{T_l - T_s} - \frac{T(x, t) - T_s}{T_l - T_s} = \frac{T(x, t + \Delta t) - T(x, t)}{T_l - T_s} \\ &= \frac{1}{T_l - T_s} \sum_{i=0}^8 [g_i(x, t + \Delta t) - g_i(x, t)] \end{aligned} \quad (2.16)$$

By substituting Equation (2.16) into Equation (2.14) and then into Equation (2.12) and reordering the collision term for a specific particle, the resultant equation will be

$$\begin{aligned} g_i(x, t + \Delta t) + \frac{w_i L}{c_p (T_l - T_s)} \sum_{j=0}^8 g_j(x, t + \Delta t) &= (1 - \omega \Delta t) g_i(x, t) + \omega \Delta t g_i^{eq}(x, t) \\ &+ \frac{w_i L}{c_p (T_l - T_s)} \sum_{j=0}^8 g_j(x, t) \end{aligned} \quad (2.17)$$

By substituting the temperature from Equation (2.5) the collision term can be defined as

$$g_i(x, t + \Delta t) + \frac{w_i L}{c_p (T_l - T_s)} \sum_{j=0}^8 g_j(x, t + \Delta t) = (1 - \omega \Delta t) g_i(x, t) + \omega \Delta t g_i^{eq}(x, t)$$

$$+ \frac{w_i L}{c_p(T_t - T_s)} T(x, t) \quad (2.18)$$

By solving for $g_i(x, t + \Delta t)$, the new distribution functions can be implicitly determined from data of the previous time step without iterations.

Note that the formulation stated by Equation (2.18) is not equivalent to the classical modified capacitance method which would have resulted by directly substituting Equation (2.15) into Equations (2.2) and (2.3). An LB discretization of E (2.1) with the source term treated as an additional capacitance yields an inefficient and poorly accurate algorithm, something that was verified with several test simulations. This is due to the introduction of dissimilar diffusivities between regular and interface cells and the fact that the latent heat is not properly weighted among the distribution functions, as is done in Equation (2.12). Observe also that although the implicit treatment of the latent heat term was facilitated by the simple form of Equation (2.15), a similar approach can be followed for more general dependencies of the fraction of liquid including the treatment of solute transport. In these cases, it is possible to express at least part of the fraction of liquid relation in terms of the temperature by using the liquidus line of the phase diagram and the solute conservation equations, as was done for example in Reference [13] in the context of a mixture formulation.

2.2.2.2 LBM boundary conditions

Defining consistent boundary conditions is crucial in LBM and many studies have been done to find the appropriate ways to apply various types of boundary conditions in lattice Boltzmann simulations. Here two different types of thermal boundary conditions including Dirichlet and Neumann conditions will be discussed.

2.2.2.2.1 Dirichlet boundary conditions

For boundaries aligned parallel to the coordinate axes, the distribution functions are not known in three directions. For example g_1 , g_5 and g_8 are unknown at the west wall as it is shown in Figure 2.1. The unknown distribution functions can be determined using the other known distribution functions and the known constant temperature boundary condition. It is assumed that the unknown distribution functions are of the form $g_i = w_i g'$, where g' is the residual temperature needed to satisfy the constant temperature at the boundary [14]. According to Equation (2.5), the prescribed temperature on the west wall can be written as:

$$T_B = \sum_{i=0}^8 g_i = g_0 + g_2 + g_3 + g_4 + g_6 + g_7 + g'(w_1 + w_5 + w_8) \quad (2.19)$$

Then the residual temperature can be calculated as

$$g' = \frac{T_B - (g_0 + g_2 + g_3 + g_4 + g_6 + g_7)}{w_1 + w_5 + w_8} = 6[T_B - (g_0 + g_2 + g_3 + g_4 + g_6 + g_7)] \quad (2.20)$$

Finally, the unknown distribution functions can be determined using the weighting factors

$$g_1 = w_1 g' = \frac{1}{9} g', \quad g_5 = w_5 g' = \frac{1}{36} g', \quad g_8 = w_8 g' = \frac{1}{36} g' \quad (2.21)$$

2.2.2.2.2 Neumann boundary condition

The Neumann boundary condition requires prescribing the heat flux or applying a convective heat transfer coefficient. In one dimension, this can be written as

$$-k \frac{\partial T}{\partial x} = -\dot{q} + h(T_{surface} - T_{\infty}) \quad (2.22)$$

where \dot{q} is the prescribed heat flux, h is the heat transfer coefficient, $T_{surface}$ is the surface temperature, T_∞ is the ambient temperature and $\frac{\partial T}{\partial x}$ is the temperature gradient. Considering the known temperature gradient at the surface, the temperature at the boundary can be determined using a three-point finite difference scheme [15]

$$T(x_0) = \frac{2}{3} \frac{\partial T}{\partial x} \bigg|_{x=x_0} + \frac{4}{3} T(x_0 + \Delta x) - \frac{1}{3} T(x_0 + 2\Delta x) \quad (2.23)$$

where x_0 corresponds to the location of the boundary. Then, the unknown distribution functions at the boundary can be calculated using the same scheme used to apply Dirichlet boundary condition.

It should be noted that a similar procedure can be employed to impose the boundary conditions at the corners considering the fact that the distributions functions are unknown in five directions at the corners (see Figure 2.1).

2.2.2.3 Numerical procedure

The sequence in which the numerical calculations are done is very important. Typically, the geometry, physical properties, initial and boundary conditions and LBM parameters, including lattice spacing and relaxation time should be defined at first. The equilibrium distribution functions are initially obtained using the prescribed temperature according to Equation (2.8) and initial distribution functions, $g_i(x,0)$, are defined as

$$g_i(x, 0) = g_i^{eq}(x, 0) \quad (2.24)$$

Then, the following steps are repeated in each time step.

1. Apply boundary conditions
2. Compute equilibrium distribution functions using Equation (2.8)

3. Collision:

If $T > T_l$ or $T < T_s$; Calculate relaxation using Equation (2.11)

If $T_s < T < T_l$; Calculate relaxation using Equation (2.18)

4. Calculate temperature using Equation (2.5)

5. Streaming

It should be noted that in contrast to previous explicit methods, the distribution functions in the collision step can be implicitly calculated by solving a small (9×9) system of linear equations at each node, and iterations and convergence criterion are not needed. Another important point is that except for the streaming step, all other steps are completely local and particles do not interact with the adjacent particles. During streaming step, the particles only interact with their nearest neighboring particles in the streaming step. This is the property which makes the method very appropriate for parallelization purposes.

2.3 Verification and discussion

In order to investigate the applicability and accuracy of the model, three different problems including one-dimensional melting of a pure metal, and one-dimensional and two-dimensional solidification of a binary alloy are solved and the obtained results are compared with analytical and FEM results.

2.3.1 One-dimensional melting of a pure metal

Melting of a semi-infinite slab of pure aluminum is simulated in one-dimension. The thermo-physical properties of pure aluminum are listed in Table 2.1 and the schematic of the problem is shown in Figure 2.2. The slab is initially assumed to be in the

uniform temperature of 600 °C. Then, it is assumed that a constant temperature of 750 °C is imposed to the left wall. The problem is considered one-dimensional since the side walls are insulated and heat transfer occurs only in one dimension. In order to compare the numerical results with the available analytical solutions, the length of the slab is considered 10 cm which is long enough to satisfy the semi-infinity assumption for the considered times and locations. The lattice spacing, Δx , and the relaxation parameter, ω , were respectively adopted as 0.1 mm and 1.0 for all simulations.

Table 2.1 Thermo-physical properties of the studied materials.

Material	Density (kg/m ³)	Conductivity (W/m.°C)	Specific Heat (J/kg.°C)	Latent Heat (J/kg)	Liquidus Temperature (°C)	Solidus Temperature (°C)
Pure Al	2698.9	210.0	900.0	386.9×10 ³	660.0	660.0
Al-3%Cu	2475.0	30.0	500.0	271.2×10 ³	652.0	596.0

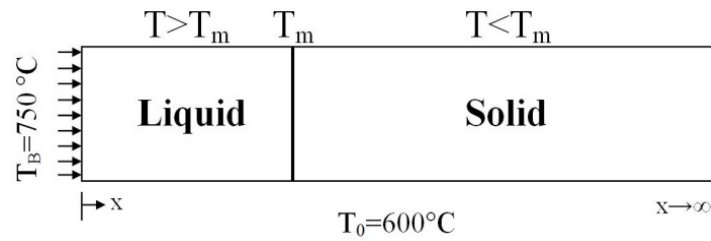


Figure 2.2 Schematic of the one-dimensional melting of the pure material showing coordinates, initial and boundary conditions, liquid and solid zones, and the interface position.

For melting of a semi-infinite slab, initially at a uniform temperature $T_0 \leq T_m$, by imposing a constant temperature $T_B > T_m$ on the face $x=0$, the analytical solution is given as follows [16]. The solid-liquid interface location has the form

$$X(t) = 2\lambda\sqrt{\alpha t} \quad (2.25)$$

Temperature in the liquid region $0 < x < X(t)$, $t > 0$ is given by

$$T(x, t) = T_B - (T_B - T_m) \frac{\text{erf}(\frac{x}{2\sqrt{\alpha t}})}{\text{erf} \lambda} \quad (2.26)$$

and temperature in the solid region $x > X(t)$, $t > 0$ can be calculated as

$$T(x, t) = T_0 + (T_m - T_0) \frac{\text{erfc}(\frac{x}{2\sqrt{\alpha t}})}{\text{erfc}(\lambda)} \quad (2.27)$$

Here λ is the solution to the transcendental equation

$$\frac{St_l}{\exp(\lambda^2)\text{erf}(\lambda)} - \frac{St_s}{\exp(\lambda^2)\text{erfc}(\lambda)} = \lambda\sqrt{\pi} \quad (2.28)$$

where

$$St_l = \frac{c_p(T_B - T_m)}{L} \quad (2.29)$$

and

$$St_s = \frac{c_p(T_m - T_0)}{L} \quad (2.30)$$

Figure 2.3 shows the thermal histories of the points located at 1, 5, 10 and 20 millimeters from the hot wall. The melting process at the points close to the hot wall begins shortly after the boundary conditions are imposed. It can be seen that the heating

rate becomes slower as the distance from the hot wall increases. A change in the slope of the curves can be seen at the melting temperature. The cause of this change is the latent heat released due to phase transformation. However, because of high heating rates at the points close to the hot wall, the slope change is not considerable at these points.

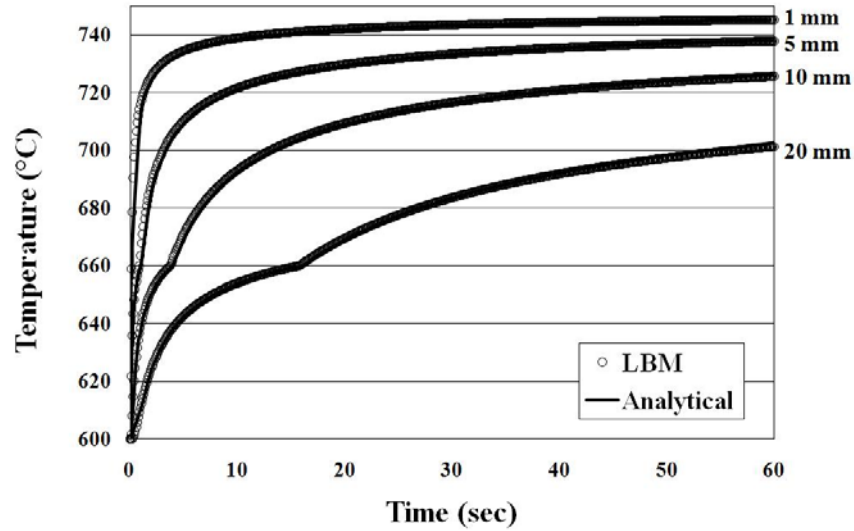


Figure 2.3 Comparison between LBM and analytical thermal histories of the points located at 1, 5, 10, and 20 mm from the hot wall for the one-dimensional pure metal melting problem.

The temperature profiles at different times are illustrated in Figure 2.4. Again, the slope change due to phase change is observed. A good consistency can be seen between LBM and analytical results in both thermal histories and temperature profiles which indicates the accuracy of the LBM model. It should be noted that since the model used for LBM simulations is not actually semi-infinite, the results gradually diverge from analytical solution as either time or distance from the hot wall increases. However, even

in this condition, the maximum relative error at long times and distances was less than 2 percent.

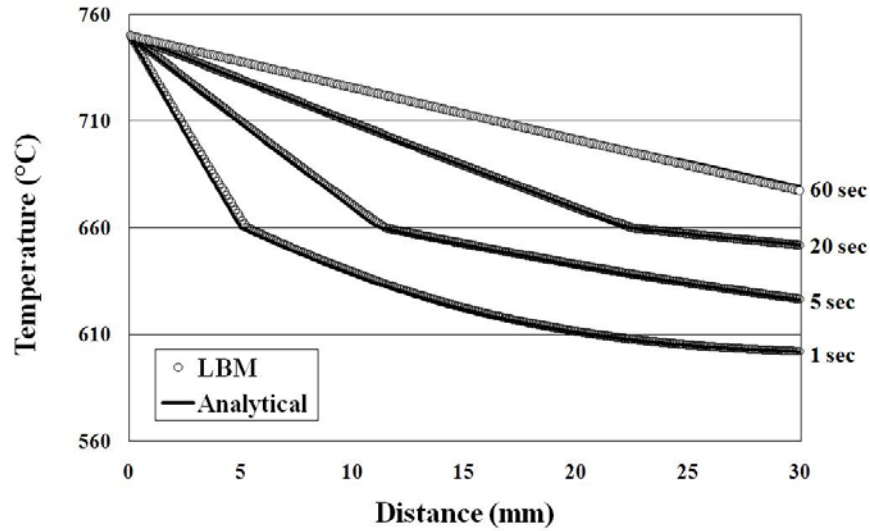


Figure 2.4 Comparison between LBM and analytical solutions for temperature profiles after 1, 5, 20, and 60 seconds for the one-dimensional pure metal melting problem.

Figure 2.5 compares the LBM and analytical solutions for the interfacial position. Again, very good agreement is shown between LBM and analytical solutions which suggests that the current LB model can precisely solve the one-dimensional phase change problem. The relative difference between FEM and LBM results was less than 0.2 percent.

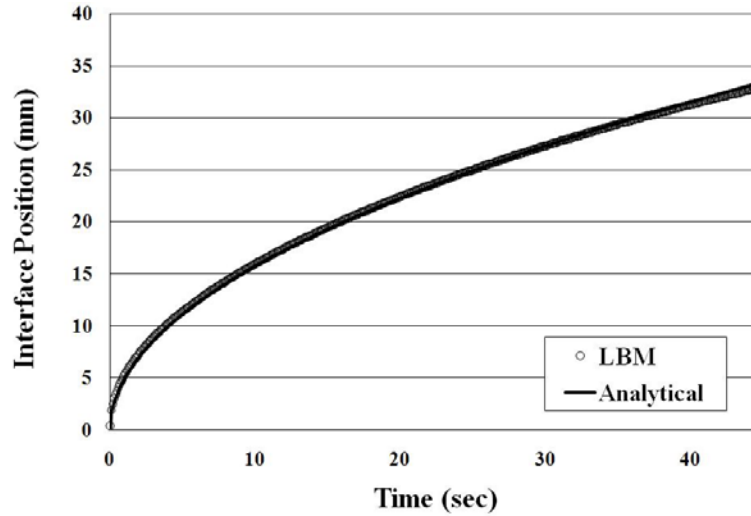


Figure 2.5 LBM and analytical solutions of the interfacial position for the one-dimensional pure metal melting problem.

2.3.2 One-dimensional solidification of a binary alloy

Solidification of a binary alloy in one dimension was simulated. It should be noted that this solution is not practically correct because solute transport which is a major mechanism in solidification of binary alloys has been neglected. However, since phase change occurs in a temperature range instead of a temperature point, which is similar to what happens in binary alloys, an Al-Cu binary alloy was considered for the study. Table 2.1 shows the thermo-physical properties of the binary alloy considered in this study and Figure 2.6 illustrates the schematic of the problem. The slab is initially at the uniform temperature $T_0=700^{\circ}\text{C}$. Then a constant heat flux $\dot{q}=-150000 \text{ W/m}^2$ is imposed on the left wall. The length of the slab is 50 millimeters and the end wall is insulated. Here phase change occurs in a range of temperature instead of a single temperature. This means that there is a so called mushy zone which is neither completely solid nor completely liquid and contains a mixture of solid and liquid phases.

LBM results for this case are verified against FEM solutions. FEM simulations are carried out using the commercial software ANSYS 10.0. The quadrilateral bilinear elements PLANE55 were used for meshing the model. The mesh size was selected fine enough to yield converged stable results. An enthalpy formulation is used to simulate phase change phenomenon using FEM.

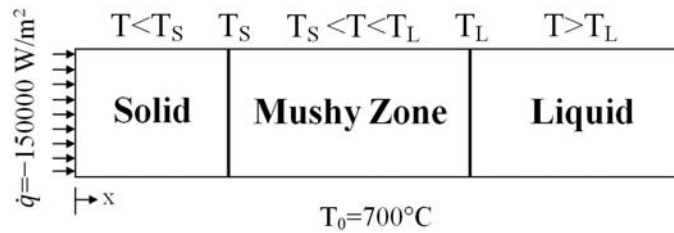


Figure 2.6 Schematic of the one-dimensional solidification of an Al-3%Cu alloy showing coordinates, initial and boundary conditions, liquid, solid and mushy zones, and the interfacial positions.

Solidification starts from the left cold wall and progresses through the slab. Figure 2.7 shows the cooling history of different points located at 1, 10, and 25 millimeters from the hot wall. Unlike the previous problem in which the phase change latent heat was released in a single temperature, here it is released in a range of temperature. Hence a sharp change in the slope of the curve cannot be seen here, but a gradual slope change can still be observed.

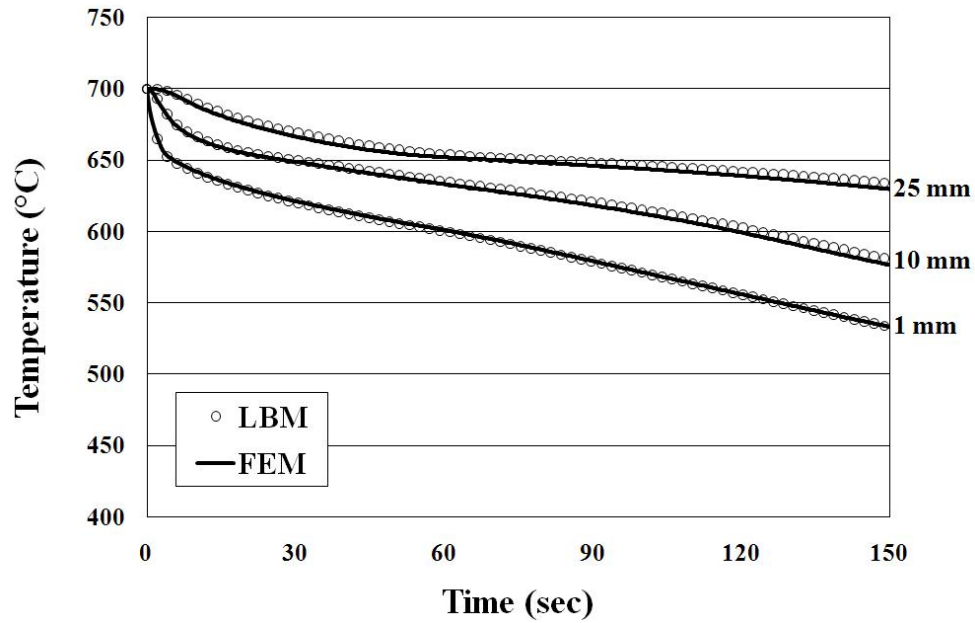


Figure 2.7 Comparison between LBM and FEM cooling curves of the points located at 1, 10, and 25 millimeters from the cold wall for the one-dimensional binary alloy solidification problem.

Figure 2.8 shows the temperature profiles at different times after the boundary conditions are imposed. As the time increases, the temperature decreases throughout the slab and the solidified front progresses. Very good agreement can be observed between LBM and FEM results in cooling curves and temperature profiles.

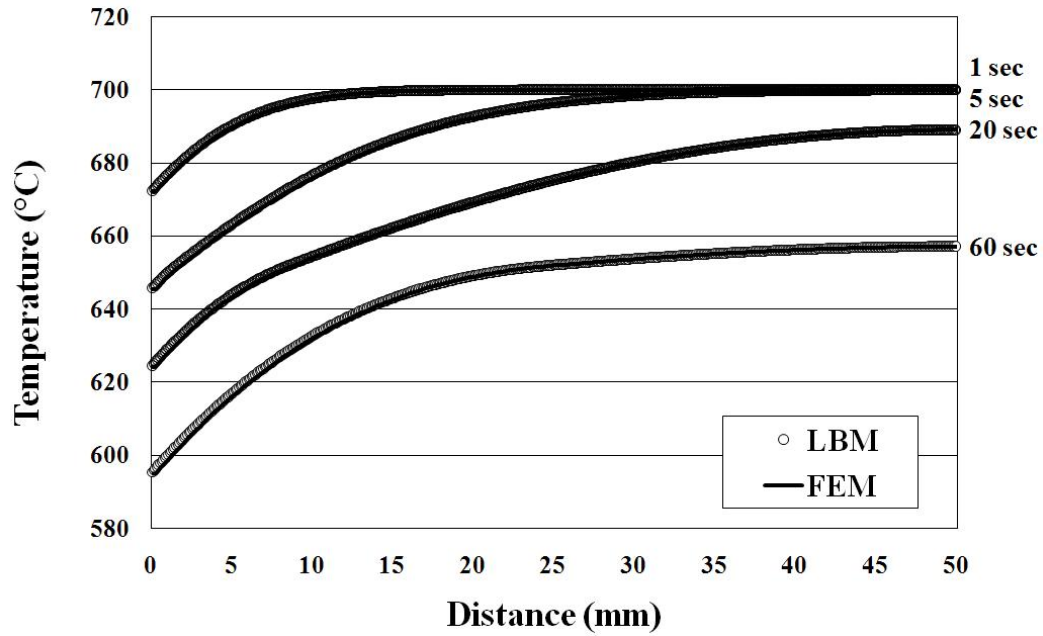


Figure 2.8 Comparison between LBM and FEM solutions for temperature profiles after 1, 5, 20, and 60 seconds for the one-dimensional binary alloy solidification problem.

LBM and FEM solutions for liquid/mushy zone (L/M) and mushy zone/solid (M/S) interfacial positions are compared in Figure 2.9. The L/M curve is sharper than M/S curve which implies that the speed of L/M interface is faster than M/S interface. Since the end wall is insulated, both interfaces are coincident after a time around 300 seconds. The excellent consistency observed between LBM and FEM results indicates the accuracy of the model for predicting phase change behavior in one-dimensional solidification problems when phase change occurs in a range of temperature.

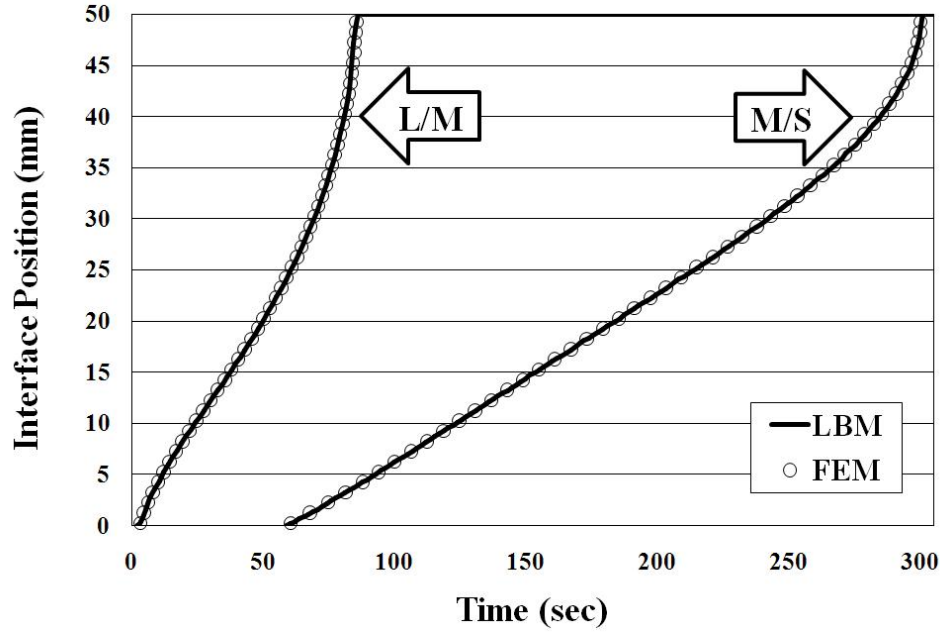


Figure 2.9 LBM and FEM solutions of the liquid/mushy zone (L/M) and mushy zone/solid (M/S) interfacial positions for the one-dimensional binary alloy solidification problem.

2.3.3 Two-dimensional solidification of a binary alloy

The material considered in this case is similar to the previous case but the boundary conditions are more complex and non-symmetric creating a two dimensional problem. Consider an infinite slab with a square cross section of $40 \times 40 \text{ mm}^2$. Since the slab is infinite, heat transfer can be neglected in the longitudinal (z) direction and the problem is assumed two-dimensional. The slab is initially at the uniform temperature $T_0 = 700^\circ\text{C}$. Then, constant heat fluxes equal to $-120,000$, $-100,000$ and $-80,000 \text{ W/m}^2$ are imposed on east, south, and west walls respectively. A convective heat transfer condition with the coefficient $h = 100 \text{ W/m}^2\text{°C}$ and ambient temperature $T_\infty = 25^\circ\text{C}$ is also considered for the north wall. Figure 2.10 shows the schematic of this problem. Again, the LBM solution is verified against an FEM solution obtained with ANSYS software.

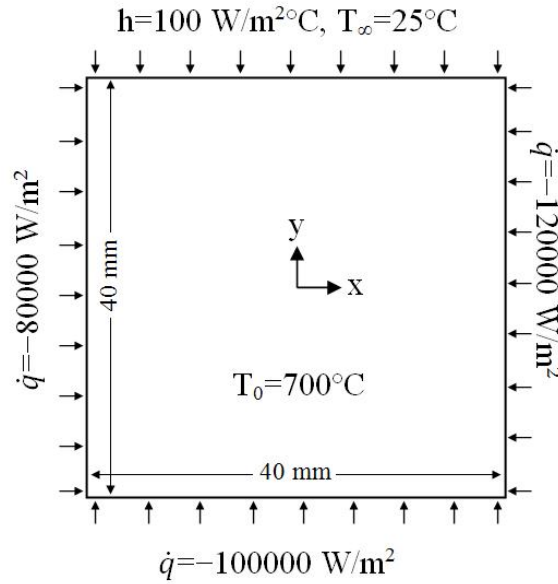


Figure 2.10 Schematic of the two-dimensional solidification of the Al-3%Cu binary alloy showing coordinates, dimensions, initial and boundary conditions.

Figure 2.11 shows the cooling history of a point located at the center of the slab. The slope change due to phase transformation in the mushy zone is well distinguishable in this case. As the temperature reaches the liquidus temperature, the cooling rate decreases owing to latent heat and once the phase change is completed at solidus temperature, the cooling rate increases. A very good agreement is shown between LBM and FEM solutions. The relative difference in this case was less than 0.15 percent.

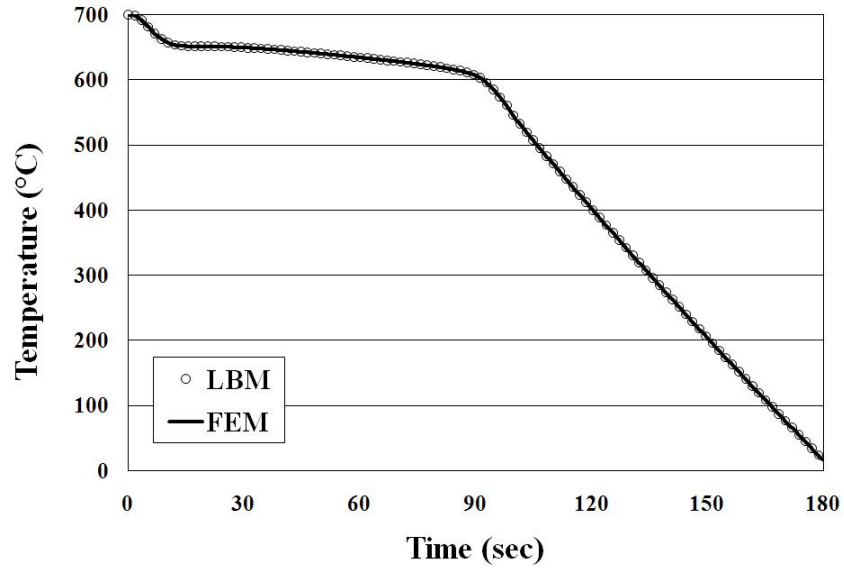


Figure 2.11 Comparison between LBM and FEM cooling curve of the point located at the center of the model for the two-dimensional binary alloy solidification problem.

The temperature profiles along x and y axes are depicted in Figure 2.12 at different times after the process begins. Even though the boundary conditions are non-symmetric, the developed model has been able to precisely capture the temperature variations in the slab.

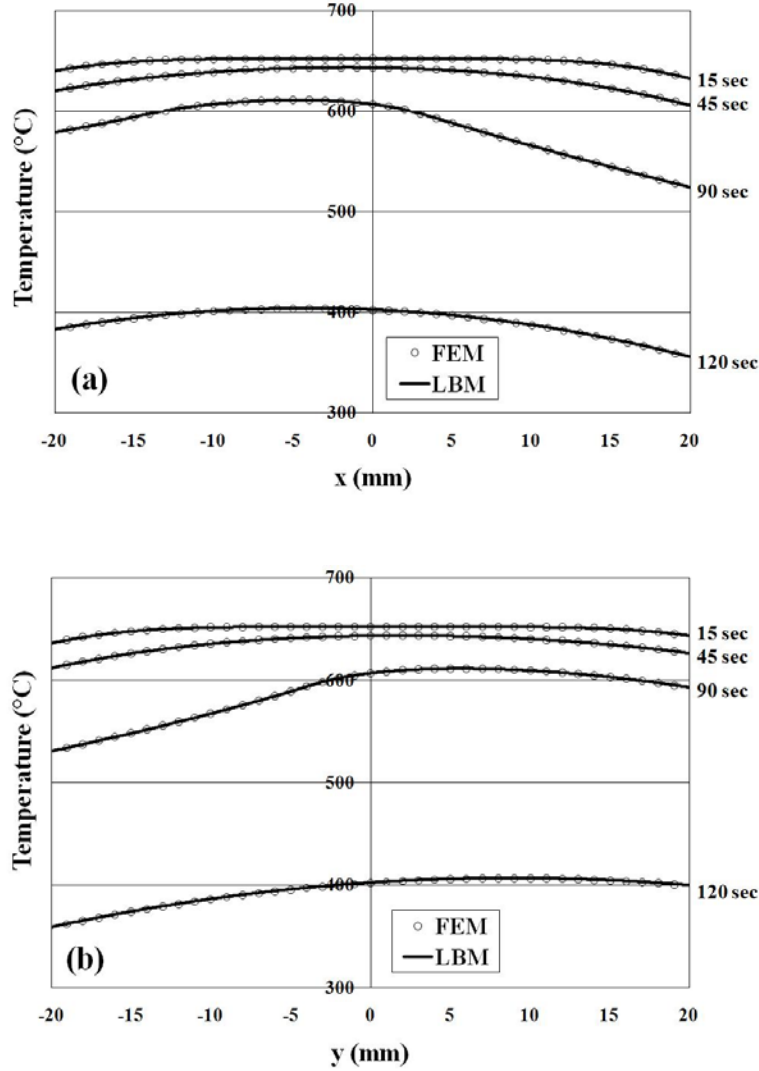


Figure 2.12 Comparison between LBM and FEM temperature profiles after 15, 45, 90, 120 seconds for the two-dimensional solidification problem.

The profiles are shown along (a) x axis, and (b) y axis.

Figure 2.13 illustrates the color contours comparing LBM and FEM solutions for temperature distribution after 15, 45, 90 and 120 seconds. Cooling process starts from the cold boundary wall. The minimum temperature is observed at the southeastern corner where the highest heat transfer happens. The hottest spot is initially located at the center

of the slab, but it migrates to the northwestern corner where the mildest heat transfer happens.

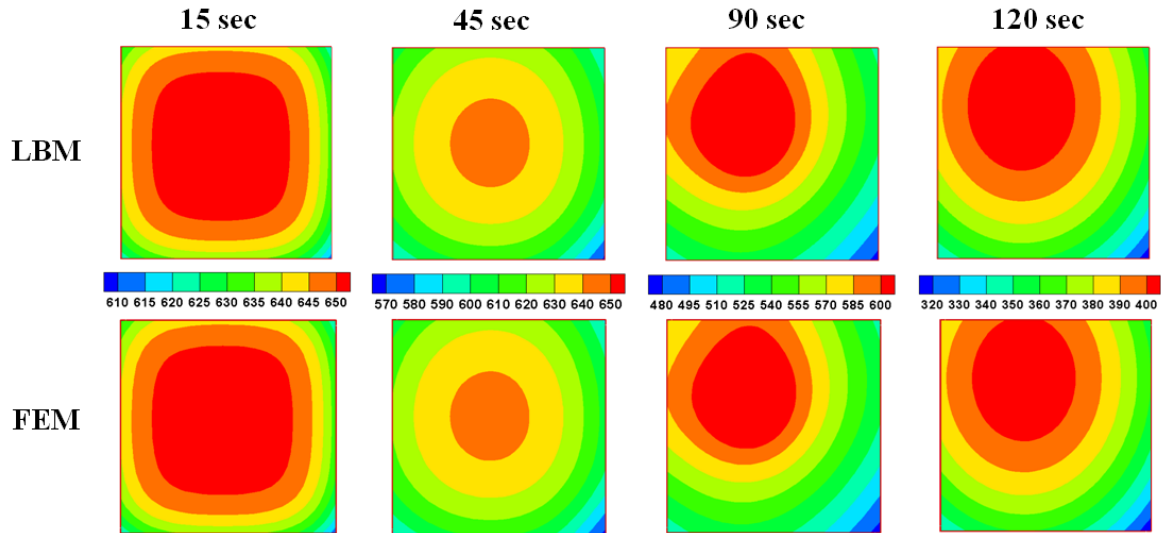


Figure 2.13 Color contours comparing LBM and FEM temperature distributions at different times for the two-dimensional solidification problem.

Figure 2.14 shows the color contours for solidified fractions at different times. It can be seen that solidification starts from cold boundary walls and progresses through the center. After 15 seconds, there is still a completely liquid region at the center. At $t=90$ seconds, some completely solidified regions are observed at the corners while all other regions are mushy. After 90 second most of the slab is solidified except for a small region at the hot spot which contains less than 40 percent liquid. The contours for at $t=120$ seconds shows that the slab is entirely solid at this time. An excellent consistency is observed between LBM and FEM contours. The agreement between LBM and FEM contour lines at the corners is also noteworthy. Considering the complicated boundary conditions applied in this simulation, this consistency indicates the ability and reliability

of the current model for precisely solving heat conduction problem with phase change in two-dimensions.

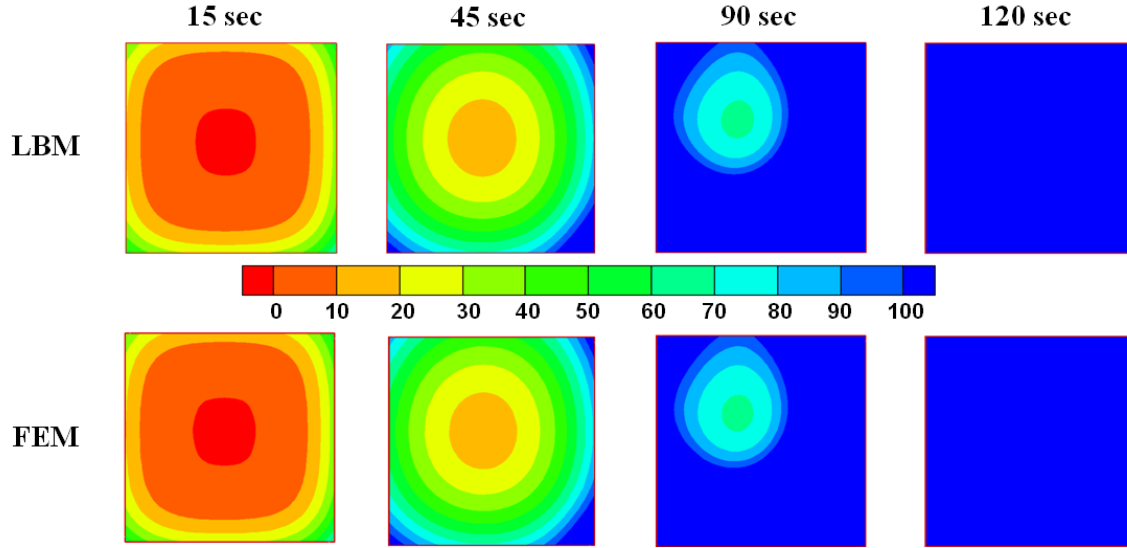


Figure 2.14 Color contours comparing LBM and FEM solid percentages at different times for the two-dimensional solidification problem.

2.3.4 Comparison of computational performance in LBM and FEM

In order to compare the computational efficiency of LBM and FEM, the problem described in the previous section (2.3.3) was solved for different domain sizes using both LBM and FEM. A lattice spacing of $\Delta x=1$ mm with relaxation parameter $\omega=1$ was used for all simulations in this part. Identical time step, grid size, initial and boundary conditions were adopted for both LBM and FEM cases and all simulations were run for 60 seconds on a laptop computer with a 2 GHz Core 2 Duo CPU and 1 GB of RAM. Bilinear quadrilateral elements and a fast iterative solver were used for the FEM calculations, in order to favor its performance. Four different square domains with 20, 50,

100, and 150 grids in each side were examined. Figure 2.15 compares the CPU times of LBM and FEM models with respect to the total number of cells/elements in the domain. The results indicate that the present LBM model offers much better computational performance than FEM. The efficiency of the LBM becomes more obvious as the domain size increases. The reason is that unlike FEM, LBM is a local method and does not require the assembly of a large global matrix and solution of system of equations that grows with domain size.

It should be noted that the real advantages of LBM appear when convection effects are incorporated, something that is demonstrated in [17]. Another important computational advantage of LBM is that, due to locality, the needed communication and passage of information between processors reduces significantly and LBM can be parallelized and scaled much better than FEM. This feature is being exploited in a work in progress by the authors.

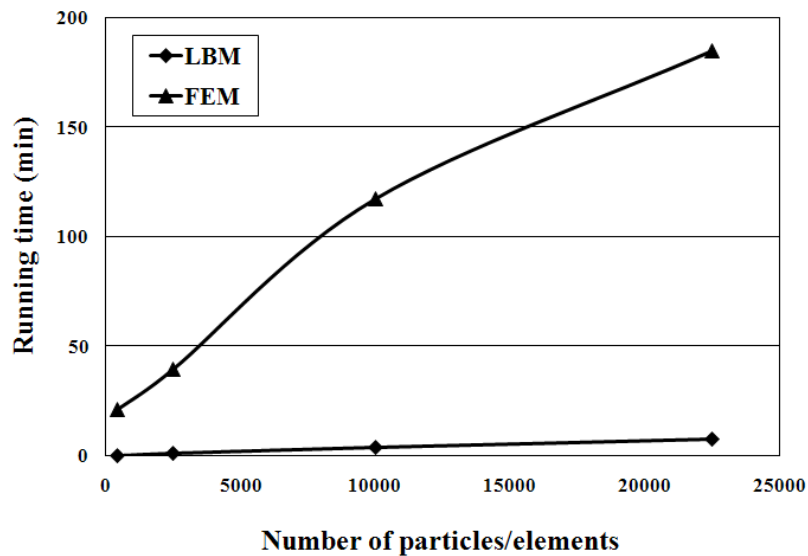


Figure 2.15 Running time of LBM and FEM models for different domain sizes.

2.4 Conclusions

A new algorithm to solve the LB equation for the heat conduction problem with solid/liquid phase change was developed. While previous works used explicit schemes, the current model uses an implicit scheme to deal with the latent heat source term of the energy equation. The Bhatnagar-Gross-Krook (BGK) approximation with a D2Q9 lattice was applied and different boundary conditions including Dirichlet and Neumann boundary conditions were considered. Three validation examples including one-dimensional melting of pure Al, and one-dimensional and two-dimensional solidification of Al-3%Cu were solved. A very good agreement between LBM, analytical, and FEM solutions was found for all examples when comparing thermal histories, temperature profiles and interfacial locations. Even for non-symmetric mixed boundary conditions, a very good accuracy was demonstrated. In addition, CPU time comparisons demonstrated that the current LBM model outperforms FEM in computational efficiency. It should be noted that while most previous works used fictitious physical properties, real material properties were employed in this study. Solving this problem with real material properties using an explicit approach is cause of convergence issues, requiring a finer mesh size, smaller time steps, more iterations and higher computational costs. From this point of view, the implicit scheme developed in this work is computationally more efficient than previous explicit schemes. On the other hand, implicit methods require an extra computation (solving the system of equation), which for this case is a small system of 9×9 equations. Note also that using D2Q5 lattice is enough for energy and mass transport simulations which will make the presented model even more efficient, because a smaller system of 5×5 equations is needed to be solved. However, whether one should use an

explicit or implicit method depends upon the problem to be solved, as for some problems limitation in the time step and mesh size is not the main issue. Considering the special capabilities of LBM, like simplicity of implementation, stability, accuracy, local characteristic, and inherent parallel structure, the proposed model offers a great potential for simulating large scale heat and mass transfer phenomena incorporating phase transformations.

The content of this chapter was published in International Journal of Heat and Mass Transfer [18] and also presented in the ASME Applied Mechanics and Materials Conference [19].

2.5 References

- [1] D. Wolf-Gladrow, A lattice Boltzmann equation for diffusion, *Journal of Statistical Physics* 79 (5–6) (1995) 1023–1032.
- [2] G. De Fabritiis, A. Mancini, D. Mansutti, S. Succi, Mesoscopic models of liquid/solid phase transitions, *International Journal of Modern Physics C* 9 (8)(1998) 1405–1415.
- [3] R. G. M. van der Sman, M. H. Ernst, A. C. Berkenbosch, Lattice Boltzmann scheme for cooling of packed cut flowers, *International Journal of Heat and Mass Transfer* 43 (4) (2000) 577–587.
- [4] W. Miller, S. Succi, A lattice Boltzmann model for anisotropic crystal growth from melt, *Journal of Statistical Physics* 112 (2002) 173–186.
- [5] E. Semma, M. El Ganaoui, R. Bennacer, A. A. Mohamad, Investigation of flows in solidification by lattice Boltzmann method, *International Journal of Thermal Sciences* 47 (3) (2008) 201–208.
- [6] W.-S. Jiaung, J.-R. Ho, C.-P. Kuo, Lattice Boltzmann method for the heat conduction problem with phase change, *Numerical Heat Transfer, Part B* 39 (2001) 167–187.
- [7] D. Chatterjee, S. Chakraborty, An enthalpy-based lattice Boltzmann model for diffusion dominated solid-liquid phase transformation, *Physics Letters A* 341 (1–4) (2005) 320–330.
- [8] D. Chatterjee, S. Chakraborty, A hybrid lattice Boltzmann model for solid-liquid phase transition in presence of fluid flow, *Physics Letters A* 351 (4–5) (2006) 359–367.
- [9] D. Chatterjee, S. Chakraborty, An enthalpy-source based lattice Boltzmann model for conduction dominated phase change of pure substances, *International Journal of Thermal Sciences* 47 (2008) 552–559.
- [10] D. Chatterjee, An enthalpy-based thermal lattice Boltzmann model for non-isothermal systems, *Europhysics Letters* 86 (1) (2009) 14004.
- [11] D. Chatterjee, Lattice Boltzmann simulation of incompressible transport phenomena in macroscopic solidification processes, *Numerical Heat Transfer, Part B: Fundamentals* 58 (1) (2010) 55–72.
- [12] J. Bhatnagar, E. P. Gross, M. K. Krook, A model for collision processes in gases: I. Small amplitude processes in charged and neutral one-component system, *Physical Review* 94(3) (1954) 511–525.

- [13] S.D. Felicelli, J.C. Heinrich, D.R. Poirier, Finite element analysis of directional solidification of multicomponent alloys, *International Journal of Numerical Methods in Fluids*, 27 (1998) 207-227.
- [14] Michael C. Sukop and Daniel T. Thorne, *Lattice Boltzmann Modeling; an Introduction for Geoscientists and Engineers*, Springer-Verlag, Berlin-Heidelberg (2006).
- [15] C.-H. Liu, K.-H. Lin, H.-C. Mai, C.-A. Lin, Thermal boundary conditions for thermal lattice Boltzmann simulation, *Computers & Mathematics with Applications* 59(7) (2010) 2178–2193.
- [16] V. Alexiades, A. D. Solomon, *Mathematical Modeling of Melting and Freezing Processes*, Taylor & Francis (1993).
- [17] H. Yin, S. D. Felicelli, L. Wang, Simulation of dendritic microstructure with lattice Boltzmann and cellular automaton methods, *Acta Materialia*, 59 (2011) 3124-3136.
- [18] M. Eshraghi, S. D. Felicelli, An implicit lattice Boltzmann model for heat conduction with phase change, *International Journal of Heat and Mass Transfer*, 55 (2012) 2420–2428.
- [19] M. Eshraghi-Kakhki, S. D. Felicelli, L. Wang, An implicit lattice Boltzmann model for heat conduction incorporating phase change, *The ASME Applied Mechanics and Materials Conference*, Chicago, IL (2011).

CHAPTER III

THREE DIMENSIONAL SIMULATION OF SOLUTE-DRIVEN DENDRITE GROWTH USING LATTICE BOLTZMANN AND CELLULAR AUTOMATON METHODS

3.1 Introduction

Dendritic growth is the primary form of crystal growth observed in most metallic alloys. The material properties strongly depend on the shape, size, orientation and composition of the dendritic matrix formed during solidification. Therefore, understanding and controlling the dendritic growth is vital in order to predict and achieve the desired microstructure and properties.

Despite the significant advances in numerical models and computational power, due to complexity and extreme memory demands, 3D simulation of dendritic growth is still challenging. Finite element (FE), finite difference (FD) and finite volume (FV) are the methods commonly used by most researchers in order to solve the transport equations. Nevertheless, the lattice Boltzmann method (LBM) is increasingly emerging as a powerful technique for simulating flows in complex geometries. Proponents of the LBM consider this method to have the potential to become a versatile platform that is superior over the existing continuum-based methods [1]. The LBM, is an ideal approach for scale-bridging simulations. Because of the microscopic origin, the LBM has many advantages over conventional methods, including simple local-type calculations, easy

handling of complex geometry and boundary conditions, good accuracy and numerical stability, constitutive versatility, and efficient parallelization. The assembly and solution of large system of equations, as needed in FE models, are avoided in LB and the model can be easily extended to calculate transport phenomena in the presence of fluid flow under complicated geometric boundary conditions.

Since the basic structure of LB is very similar to CA, combination of these methods seems a natural approach. Given their local-type nature and their good scalability for many processors, a dendritic growth model based on these methods is an attractive choice for exploitation of large scale parallelization. There are a few publications on modeling dendrite growth using LB and CA. Sun *et al.* [2] introduced a two-dimensional (2D) LB-CA model for dendritic solidification. They used CA to capture the solid-liquid interface and LB to solve solute transport and fluid flow. Yin *et al.* [3] used a similar approach to simulate dendrite growth. They also solved the heat transfer using LB and compared their LB-CA model with an FE-CA model. However, 2D models are usually unable to capture all features of microstructures which are determinative in many materials properties. In this chapter, a first-time three-dimensional (3D) parallel LB-CA model is introduced for simulation of dendritic microstructures in binary alloys.

3.2 Model description

In order to simulate 3D dendrite growth, a cubic domain is considered and discretized using cubic cells. An identical mesh is employed for both LB and CA models. At the beginning of simulation, a solid seed with a predetermined crystallographic orientation is placed in a domain of undercooled molten alloy. Since the local equilibrium

composition is larger than the actual local liquid composition, solidification begins and solute is rejected to the interface to increase the liquid composition to the equilibrium composition. So, it can be said that the solidification is driven by the difference between the local equilibrium composition and the local actual liquid composition.

The governing differential equation for solute transport in liquid phase can be described as

$$\frac{\partial c_l}{\partial t} = \nabla \cdot (D_l \nabla C_l) \quad (3.1)$$

where C_l is the liquid composition, t is time, and D_l is solute diffusion coefficient in liquid. Since the solute diffusivity in the solid is several orders of magnitude smaller than in the liquid, the diffusion in the solid phase is neglected.

In LBM, the domain is discretized into a number of pseudo particles located at the nodes of the lattice and time is discretized into some distinct steps. A 3D lattice with fifteen discrete velocities, D3Q15, is used in the simulations. Figure 3.1 shows the D3Q15 lattice. The entire domain is assumed to be uniformly undercooled and the kinetics of dendrite growth is controlled solely by solute transport.

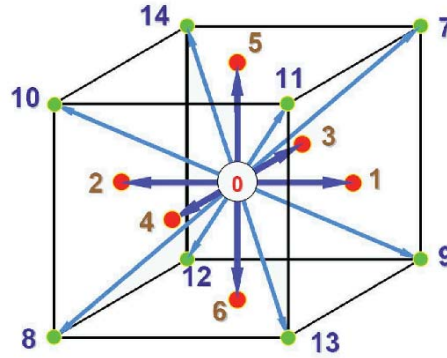


Figure 3.1 D3Q15 lattice.

The distribution function, $g_i(x,t)$, is defined as the probability of finding a particle moving in direction i . Then, the macroscopic solute concentration, $C(x,t)$, can be calculated as

$$C(x,t) = \sum_{i=0}^{14} g_i(x,t) \quad (3.2)$$

According to the BGK (Bhatnagar-Gross-Krook) approximation [4], the kinetic equation for the distribution function can be written as

$$g_i(x + e_i \Delta t, t + \Delta t) - g_i(x, t) = -\omega \Delta t (g_i(x, t) - g_i^{eq}(x, t)) \quad (3.3)$$

where e_i , Δt , and ω are discrete velocity, time step, and relaxation parameter, respectively. $g_i^{eq}(x, t)$ is the equilibrium distribution function which can be expressed as

$$g_i^{eq}(x, t) = w_i C(x, t) \quad (3.4)$$

w_i is the weighting factor in the discrete directions and is defined as follows [5]

$$w_i = \begin{cases} 16/72 & i = 0 \\ 8/72 & i = 1 - 6 \\ 1/72 & i = 7 - 14 \end{cases} \quad (3.5)$$

In the present model, dendrite growth is controlled by the difference between local equilibrium solute concentration and local actual solute concentration in the liquid. According to the equilibrium condition at the interface, the change of the fraction of solid, Δf_s , in an interface cell is calculated by [6]

$$\Delta f_s = (C_l^{eq} - C_l) / (C_l^{eq} (1 - k)) \quad (3.6)$$

where k is the partition coefficient of the solute obtained from the phase diagram and C_l is the local actual concentration of solute in the liquid and is computed by LB. Moreover, C_l^{eq} is the interface equilibrium concentration that can be calculated as [7]

$$C_l^{eq} = C_0 + \frac{T_l^* - T_l^{eq} + \Gamma wmc}{m} \quad (3.7)$$

where T_l^* is the interface temperature, T_l^{eq} is the equilibrium liquidus temperature at the initial solute concentration (C_0), m is the slope of the liquidus line in the phase diagram, Γ is the Gibbs-Thomson coefficient, and wmc is the weighted mean curvature that includes the effect of anisotropic surface energy [8] and can be calculated as

$$wmc = (3\varepsilon - 1)(\partial_x n_x + \partial_y n_y + \partial_z n_z) - 48\varepsilon(n_x^2 \partial_x n_x + n_y^2 \partial_y n_y + n_z^2 \partial_z n_z) + 12\varepsilon Q(\partial_x n_x + \partial_y n_y + \partial_z n_z) + 12\varepsilon(n_x \partial_x Q + n_y \partial_y Q + n_z \partial_z Q) \quad (3.8)$$

where ε represents the degree of anisotropy of the surface energy. Considering \hat{n} as the unit vector normal to the interface, its components can be evaluated as

$n_x = \partial_x f_s / |\nabla f_s|$, $n_y = \partial_y f_s / |\nabla f_s|$, and $n_z = \partial_z f_s / |\nabla f_s|$, where $|\nabla f_s| = \sqrt{(\partial_x f_s)^2 + (\partial_y f_s)^2 + (\partial_z f_s)^2}$. The parameter Q is defined as $Q = n_x^4 + n_y^4 + n_z^4$ [7].

The material considered in this study is Al-3wt%Cu alloy. The physical properties used in the simulations are listed in Table 3.1.

Table 3.1 Physical properties of Al-Cu alloy used in the simulations.

Density, ρ (kg m^{-3})	Diffusion Coefficient, D ($\text{m}^2 \text{s}^{-1}$)	Viscosity, μ (N s m^{-2})	Liquidus Slope, m ($^\circ\text{C wt}\%^{-1}$)	Partition Coefficient, k	Gibbs-Thomson Coefficient, Γ ($\text{m } ^\circ\text{C}$)	Degree of anisotropy, ε
2475.0	3.0×10^{-9}	0.0024	-2.6	0.17	2.4×10^{-7}	0.04

3.3 Results and discussion

3.3.1 Growth kinetics

A cubic domain with a uniform mesh size $\Delta x = 0.3 \mu\text{m}$ and a constant undercooling was used to simulate the dendrite growth. Figure 3.2 shows the morphology of the dendrite growing in a $120 \mu\text{m} \times 120 \mu\text{m} \times 120 \mu\text{m}$ domain at different time steps.

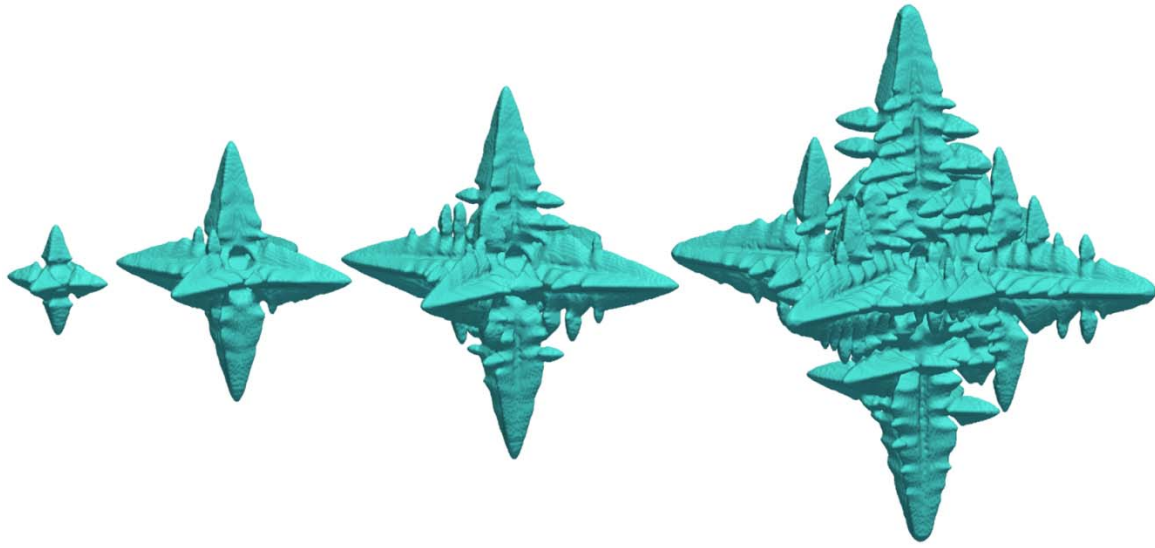


Figure 3.2 Simulated dendrite morphologies for $\Delta T = 4.5 \text{ }^\circ\text{C}$ and $\epsilon = 0.04$. From left to right, after 3, 7, 10, and 15 ms.

The simulations are conducted using a $4.5 \text{ }^\circ\text{C}$ undercooled melt and the anisotropy parameter, ϵ , equal to 0.04. At the initial stages of solidification, the primary arms grow along their crystallographic orientation without any secondary arms. As solidification proceeds, the primary arms grow and coarsen, the secondary arms start to grow perpendicular to the primary arms and the tertiary arms form perpendicular to the secondary arms afterward.

3.3.2 Model validation

For model validation, the growth features are compared with the Lipton-Glicksman-Kurz (LGK) [9, 10] analytical model for different levels of undercooling. The LGK model predicts the tip velocity and radius as a function of a selection parameter, σ^* .

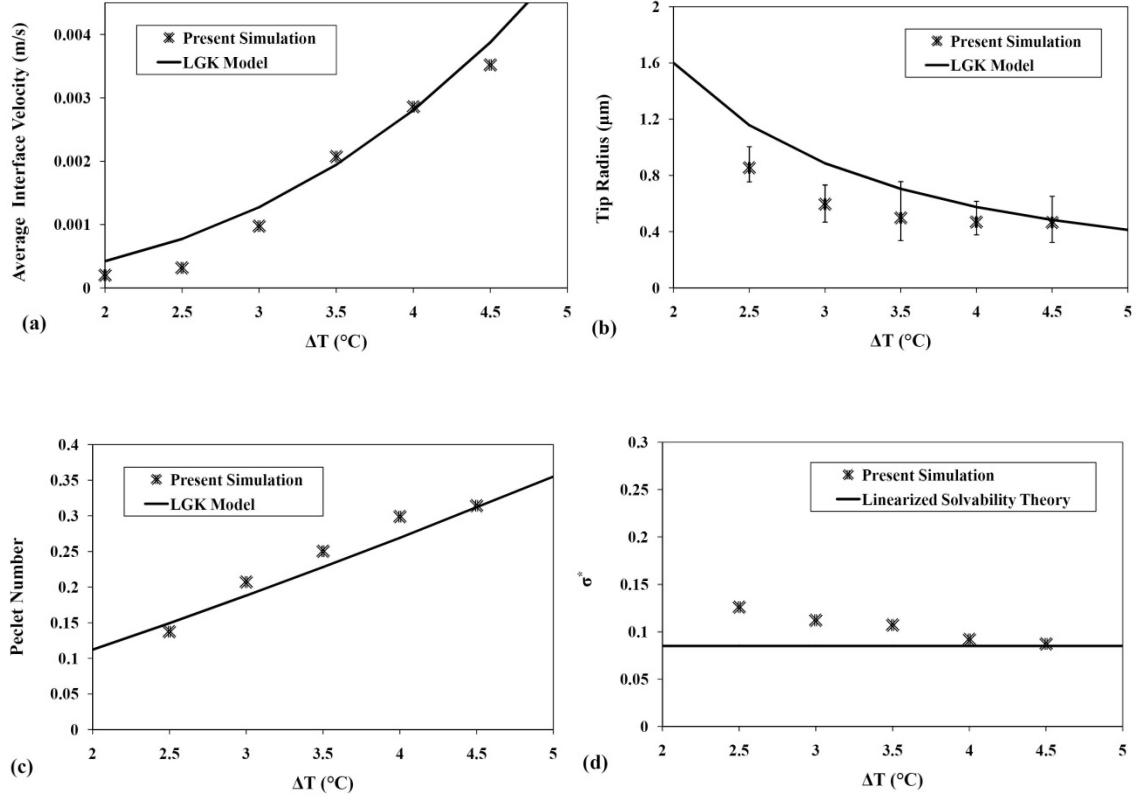


Figure 3.3 Comparison of the dendritic features simulated by the present model with the theoretical values over a range of undercoolings: (a) tip velocity, (b) tip radius, (c) Peclet number, and (d) σ^* .

According to 3D linearized solvability theory [11], the value of σ^* for $\varepsilon = 0.03$ is calculated as 0.085. Using this value, the steady state tip velocity and radius were calculated by LGK model as a function of undercooling and compared with the

simulation results. Figure 3.3 (a) compares the tip velocity calculated from the simulation with the tip velocity predicted by LGK model. The simulated tip velocity was measured by averaging the interface velocity at the tips of six primary dendrite arms. As expected, the average interface velocity increases with increasing undercooling. While some small differences can be observed, the values calculated by the present simulations show a good agreement with the LGK analytical model. In order to measure the tip radius of the simulated dendrites, 3D isosurface plots were depicted for $f_s=0.5$. Then, the 3D dendritic tips were sectioned by two different planes to provide 2D fin shapes. After fitting forth-order polynomials, the curvature at the dendritic tip was calculated as $K=d^2y/dx^2(1+(dy/dx)^2)^{-3/2}$ [12] and the tip radius was determined as $R=1/K$. The above calculations were performed for six different branches at few different time steps when dendrite growth is in the steady-state. Figure 3.3 (b) compares the tip radius measured from present simulations with the theoretical values obtained from LGK model. A relatively large variation between LGK and simulated values can be seen in the tip radius especially at low undercoolings. However, simulated and theoretical values are in the same order of magnitude and show the same trend. The discrepancy in the tip radius is caused mainly by the discretization of the dendrite tip in the CA method, which produces an inaccurate representation of the tip and large error in calculating curvature and radius. As undercooling decreases, tip radius increases, and tip curvature becomes smaller and more erroneous. Also, at low undercoolings, the dendritic shape deviates from the parabolic shape assumed in the LGK model. It is worth noting that the same problem has been observed in other studies [7, 13].

The solutal Peclet number was also calculated from the LGK theory and compared with the simulation results. The Peclet number can be calculated as $P_c = VR/(2D_l)$, where V and R are tip velocity and radius, respectively. The predicted and theoretical Peclet numbers for a range of undercoolings are presented in Figure 3.3 (c) and a good agreement is observed.

While a reasonable agreement can be found between the simulated and theoretical results, it should be noted that the LGK model is not exact and assumes a paraboloid needle tip which does not correspond with the actual dendrites. On the other hand, the selection parameter, σ^* , which has a significant influence on the results, is not well established for aluminum alloys. By knowing the dendrite tip velocity and radius, it is possible to calculate the selection parameter for different levels of undercooling. Figure 3.3 (d) compares the selection parameters calculated from the present simulations with $\sigma^* = 0.085$ obtained from 3D linearized solvability theory [11]. The values vary from 0.126 at $\Delta T = 2.0$ °C to 0.087 at $\Delta T = 4.5$ °C. The higher difference at lower undercoolings mostly comes from the error associated with measuring tip radius at those undercoolings. However, as described above, a perfect match between simulation and LGK theory should not be expected.

As another validation, the results of the present model were compared with 3D-CA and 3D-PF simulations performed by Choudhury *et al.* [13]. The simulation was done on an Al-4wt%Cu alloy and the values of undercooling and degree of anisotropy were selected to be 3.81 °C and 0.0097, respectively, to match the values employed by [13]. Table 3.2 lists the tip velocities obtained from different models. The closest tip velocities to theoretical LGK values for $\sigma^* = 0.05$, as suggested by [13] for this alloy, are obtained

respectively by: present LB-CA, CA and PF models. The better accuracy of CA models comes from the fact that the Moore neighborhood in 3D consists of 27 cells, in comparison with 9 cells in 2D. This results in better representation of the interface, and more accurate curvature calculation in 3D. A similar behavior was observed in the 3D FD-CA model presented in [7]. While it is expected that PF yields more accurate results compared to CA, a larger error is observed between PF and LGK theory. However, some considerations should be taken into account when quantitative results are sought in PF. In particular, grid spacing should be very small in order to capture the interface accurately, especially for higher undercoolings. Failure in satisfying the above condition may lead to inaccurate results. Nevertheless, as mentioned previously, the LGK model is approximate and should not be taken as an absolute benchmark solution.

Table 3.2 Comparison of dendrite tip velocities for Al-4wt%Cu alloy obtained from present LB-CA , LGK ($\sigma^*=0.05$), CA and PF models.

Method	Tip Velocity ($\mu\text{m/s}$)
Present LB-CA	1147
LGK [13]	1393
3D-CA [13]	857
3D-PF [13]	400

3.3.3 Solute distribution

Figure 3.4 depicts the solute distribution field around the dendrite after 15ms. As the solidification proceeds, the solute atoms are rejected from solid to liquid. Since the rate of solute rejection is more than the rate of diffusion, solute atoms accumulate at the interface front, as shown by higher solute concentration between the dendrite arms. At the later steps of solidification, the solute atoms may become trapped between solidified

regions and result in microsegregation. This phenomenon can be recognized in the regions close to the dendrite core in Figure 3.4.

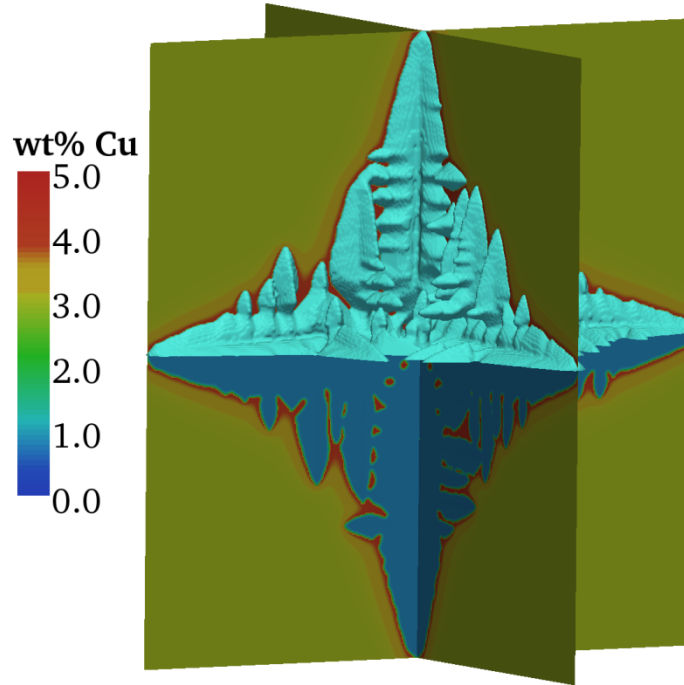


Figure 3.4 Solute concentration field around the dendrite for $\Delta T=4.5$ °C and $\varepsilon=0.04$ after 15 ms.

3.3.4 Effect of anisotropy of the surface energy

The effect of degree of anisotropy of the surface energy on growth kinetics and morphology of the dendrite is also studied as a means of qualitative validation of the model. Anisotropy is one of the most important physical phenomena that controls the kinetics of dendrite growth. Seven different values of the anisotropy parameter ranging from 0.01 to 0.07 with 0.01 increments are tested. The undercooling is considered to be 4.5 °C for all cases. Figure 3.5 shows the effect of anisotropy coefficient on morphology

and tip velocity of the dendrite. The dendrite grows faster and the tip velocity increases as the degree of anisotropy increases. By increasing the degree of anisotropy, the part of total undercooling which is controlled by interfacial anisotropy increases and results in a higher solidification rate. For large degrees of anisotropy, the dendritic arms are more enforced to follow the crystallographic directions and a branchless needle-shape dendrite with very sharp edges is obtained. On the other hand, when small values are used for the anisotropy parameter, the instability at the interface increases and the dendrite grows with well-developed side branches and relatively round edges. While the dendrite growth mostly follows the $\langle 1\ 0\ 0 \rangle$ crystallographic directions, branches start to grow in $\langle 1\ 1\ 1 \rangle$ directions when very small anisotropy parameters, less than 0.01, are applied. Another interesting aspect is showing the possibility of changing dendrite morphologies (i.e. size, arm spacing, and orientation) by changing the anisotropy and interfacial energy parameters, which may be possible by altering chemical composition of alloys. However, this needs a more extensive study as suggested by [14].

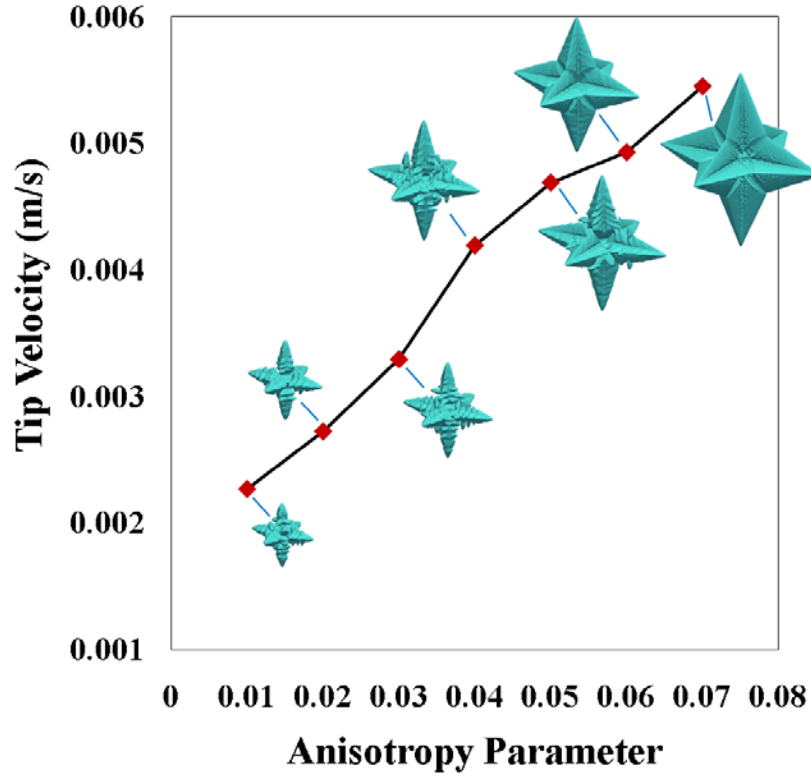


Figure 3.5 Variation of dendrite morphology and tip velocity with respect to anisotropy parameter.

3.4 Conclusions

In summary, a three dimensional LB-CA model is introduced for simulating solute-driven dendrite growth. The model successfully captures the morphology of dendritic microstructure in three dimensions. Comparing the growth features over a range of undercoolings shows a good agreement between the simulation results and the theoretical predictions. The results show that when larger anisotropy parameters are selected, a branchless dendrite with sharp edges grows with high tip velocity. On the other hand, when smaller anisotropy parameters are used, a dendrite with well-developed branches and low tip velocity is produced. Exploiting the local characteristics of both LB

and CA methods, the presented model exhibits good computational efficiency and parallel scalability, with potential for large 3D simulations of microstructural evolution in domains approaching macroscopic size.

The work of this chapter was published in Journal of Crystal Growth in 2012 [15] and was also pre-viewed and presented partially in the 2012 TMS Annual Meeting & Exhibition [16] and the International Conference on 3D Materials Science [17].

3.5 References

- [1] R. Raj, A. Prasad, P.R. Parida, S.C. Mishra, Analysis of solidification of a semitransparent planar layer using the lattice Boltzmann method and the discrete transfer method, *Numerical Heat Transfer A* 49 (2006) 279–299.
- [2] D. Sun, M.F. Zhu, S. Pan, D. Raabe, Lattice Boltzmann modeling of dendritic growth in a forced melt convection, *Acta Materialia* 57 (2009) 1755–1767.
- [3] H. Yin, S.D. Felicelli, L. Wang, Simulation of dendritic microstructure with lattice Boltzmann and cellular automaton methods, *Acta Materialia* 59 (2011) 3124–3136.
- [4] J. Bhatnagar, E. P. Gross, M. K. Krook, A model for collision processes in gases: I. Small amplitude processes in charged and neutral one-component system, *Physical Review* 94 (1954) 511–525.
- [5] A. A. Mohamad, *Lattice Boltzmann method: fundamentals and engineering applications with computer codes*, First ed., Springer, London (2011).
- [6] M. F. Zhu, D. M. Stefanescu, Virtual front tracking model for the quantitative modeling of dendritic growth in solidification of alloys, *Acta Materialia* 55 (2007) 1741–1755.
- [7] S. Pan, M. Zhu, A three-dimensional sharp interface model for the quantitative simulation of solutal dendritic growth, *Acta Materialia* 58 (2010) 340–352.
- [8] J. E. Taylor, Mean curvature and weighted mean curvature, *Acta Metallurgica et Materialia* 40 (1992), 1475–1485.
- [9] J. Lipton, M. E. Glicksman, W. Kurz, Dendritic growth into undercooled alloy melts, *Materials Science and Engineering* 65 (1984) 57–63.
- [10] J. Lipton, M. E. Glicksman, W. Kurz, Equiaxed dendrite growth at small supercooling, *Metallurgical Transactions A* 18 (1987) 341–345.
- [11] A. Barbieri, J. S. Langer, Predictions of dendritic growth rates in the linearized solvability theory, *Physical Review A* 39 (1989) 5314.
- [12] D. M. Stefanescu, *Science and engineering of casting solidification*, Kluwer Academic/Plenum Publishers, New York (2002).
- [13] A. Choudhury, K. Reuther, E. Wesner, A. August, B. Nestler, M. Rettenmayr, Comparison of phase-field and cellular automaton models for dendritic solidification in Al–Cu alloy, *Comp. Mater. Sci.* 55 (2012) 263–268.

- [14] T. Haxhimali, A. Karma, F. Gonzales, M. Rappaz, Orientation selection in dendritic evolution, *Nature Materials* 5 (2006) 660–664.
- [15] M. Eshraghi, S. D. Felicelli, B. Jelinek, Three dimensional simulation of solutal dendrite growth using lattice Boltzmann and cellular automaton methods, *Journal of Crystal Growth* 354 (2012) 129–134.
- [16] M. Eshraghi, S. D. Felicelli, Numerical modeling of dendritic growth during solidification of alloys using lattice Boltzmann and cellular automaton methods, 2012 TMS Annual Meeting & Exhibition, Orlando, FL (2012).
- [17] M. Eshraghi, S. D. Felicelli, Three dimensional simulation of dendritic solidification by lattice Boltzmann and cellular automaton methods, International Conference on 3D Materials Science, Seven Springs, PA (2012).

CHAPTER IV

THREE-DIMENSIONAL LATTICE BOLTZMANN MODELING OF DENDRITIC SOLIDIFICATION UNDER FORCED CONVECTION

4.1 Introduction

As mentioned in the previous chapter, there are few works on modeling dendritic solidification in two dimensions. However, 2D models are usually unable to capture all features of microstructures which are determinative in many materials properties. It is known that melt flow can significantly alter the growth kinetics by affecting solutal gradient around the dendrites. While melt convection is blocked by dendrite arms in two-dimensional simulations, flow can go around the 3D arms which results in a different solute distribution and dendritic morphology. Studies [1-5] have shown that the growth of dendrites in 3D is considerably different from 2D. Therefore, in order to obtain correct physical results, it is necessary to perform the simulations in 3D. In the previous chapter, the development of a three dimensional LB–CA model for simulating solute-driven dendrite growth was discussed. The model successfully captures the morphology of dendritic microstructure in three dimensions, but it does not contain the fluid flow calculations [6].

This chapter aims to introduce a three-dimensional LB–CA model for simulation of dendritic growth under forced convection. The model is verified against the available analytical solutions for diffusion-advection, and fluid flow. The results of 3D and 2D

dendrite growth simulations are compared. In addition, the change in growth kinetics and morphology of Al-Cu dendrites is studied by altering melt undercooling, alloy composition and inlet flow velocity.

4.2 Model description

In the LB model developed in this work, the time domain is divided into equal time steps while the spatial domain is discretized with a uniform 3D cubic grid. There are a few possibilities for spatial position of the fictive particles. The well-known D3Q15 lattice is employed in this work, which is a three dimensional lattice with 15 microscopic velocities; 1 residing at the center of the cube, 6 towards the cube's faces, and 8 towards the cube's corners. The discrete velocities in the D3Q15 lattice are given as:

$$\mathbf{e}_i = c \times \begin{cases} (0, 0, 0) & i = 0 \\ (\pm 1, 0, 0), (0, \pm 1, 0), (0, 0, \pm 1) & i = 1 - 6 \\ (\pm 1, \pm 1, \pm 1) & i = 7 - 14 \end{cases} \quad (4.1)$$

where $c = \Delta x / \Delta t$ is the lattice speed, Δx is lattice spacing, and Δt is time step size.

It is assumed that the temperature in the entire domain is uniform with a constant undercooling. So, heat transport is not solved and only solute diffusion and fluid flow models are included in this work. Also, solute transport in the solid phase is neglected.

The motion of an incompressible Newtonian fluid is described by the Navier-Stokes equations (NSE):

$$\rho \left(\frac{\partial \mathbf{u}}{\partial t} + \mathbf{u} \cdot \nabla \mathbf{u} \right) = -\nabla p + \nabla \cdot (\mu \nabla \mathbf{u}) \quad (4.2)$$

where ρ and \mathbf{u} are density and velocity, respectively. According to the BGK (Bhatnagar-Gross-Krook) approximation [7], the LB equation for fluid flow can be written as:

$$f_i(\mathbf{x} + \mathbf{e}_i \Delta t, t + \Delta t) - f_i(\mathbf{x}, t) = -\frac{1}{\tau_u} (f_i(\mathbf{x}, t) - f_i^{eq}(\mathbf{x}, t)) \quad (4.3)$$

where \mathbf{e}_i , and τ_u are discrete velocity, and nondimensional relaxation time, respectively. f_i is the distribution function and is defined as the probability of finding a particle at position \mathbf{x} moving in direction i . f_i^{eq} is the equilibrium distribution function:

$$f_i^{eq} = w_i \rho \left(1 + 3 \frac{\mathbf{e}_i \cdot \mathbf{u}}{c^2} + \frac{9(\mathbf{e}_i \cdot \mathbf{u})^2}{2c^4} - \frac{3u^2}{2c^2} \right) \quad (4.4)$$

w_i is the weight coefficient that for the D3Q15 lattice is given as:

$$w_i = \begin{cases} 16/72 & i = 0 \\ 8/72 & i = 1 - 6 \\ 1/72 & i = 7 - 14 \end{cases} \quad (4.5)$$

Using the Chapman-Enskog expansion, it can be proved that the LB equation is equivalent to the NSE, if the following equation is satisfied.

$$\nu = \frac{c^2 \Delta t}{6} (2\tau_u - 1) \quad (4.6)$$

Here, ν is the kinematic viscosity.

Then, the macroscopic values of density and velocity can be obtained from LB distribution functions as follows:

$$\rho = \sum_{i=0}^{14} f_i \quad (4.7)$$

$$\mathbf{u} = \frac{1}{\rho} \sum_{i=0}^{14} f_i \mathbf{e}_i \quad (4.8)$$

The solute can be transported by both diffusion and advection in the liquid. The advection-diffusion equation describes the solute transport under the effect of melt flow and diffusion:

$$\frac{\partial C_l}{\partial t} = \nabla \cdot (D_l \nabla C_l) - \mathbf{u} \nabla C_l \quad (4.9)$$

where C_l is the solute concentration and D_l is the solute diffusivity in the melt.

The equivalent LB equation for solute transport can be written as:

$$g_i(\mathbf{x} + \mathbf{e}_i \Delta t, t + \Delta t) - g_i(\mathbf{x}, t) = -\frac{1}{\tau_c} (g_i(\mathbf{x}, t) - g_i^{eq}(\mathbf{x}, t)) \quad (4.10)$$

where g_i is the solute distribution function and τ_c is the relaxation time for the solute transport model. The equilibrium distribution function, g_i^{eq} , for this model is defined as:

$$g_i^{eq} = w_i C_l \left(1 + 3 \frac{\mathbf{e}_i \cdot \mathbf{u}}{c^2} \right) \quad (4.11)$$

Then, the macroscopic solute concentration, $C_l(x, t)$, can be calculated as:

$$C_l = \sum_{i=0}^{14} g_i \quad (4.12)$$

The LB Equation (4.10) reduces to the advection-diffusion Equation (4.9), if:

$$D_l = \frac{c^2 \Delta t}{6} (2\tau_c - 1) \quad (4.13)$$

In the present model, dendrite growth is controlled by the difference between local equilibrium solute concentration and local actual solute concentration in the liquid, as described in the previous chapter. Also, a CA algorithm is used to capture new interface cells. For more details about the solid fraction calculations and capturing new interface cells, please look at Chapter III.

At the beginning of the simulation, a solid seed with a predetermined crystallographic orientation is placed in a domain of undercooled molten alloy. A uniform flow in the x-direction, with velocity magnitude U_0 , enters the domain from the west wall, as shown in Figure 4.1. The nonslip boundary condition at the solid/liquid interface is applied using the bounce-back rule for both fluid flow and solute diffusion calculations. Bounce back is one of the most interesting aspects of the LBM. Using bounce back, the incoming distribution functions at the solid particles are simply reflected back to the fluid. Using this simple method, the interaction of fluid with complex boundaries of the dendrite can be efficiently modeled. The side walls are assumed to be periodic and a zeroth extrapolation is used to simulate the open wall on the east side. Besides, all boundary walls are insulated against the solute transport. The buoyancy effect is ignored and it is assumed that the dendrite is stationary and does not move with the flow.

The non-dimensional relaxation time is chosen to be one for both fluid flow and solute transport models and the mesh spacing is $0.3 \mu\text{m}$ for all dendrite growth simulations.

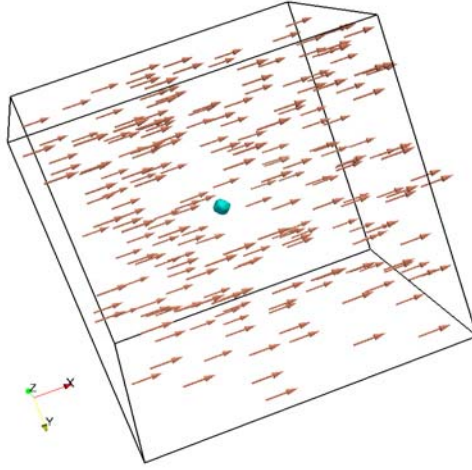


Figure 4.1 Schematic illustration of the simulation domain.

4.3 Results and discussion

4.3.1 Validation

In order to validate the fluid flow and solute transport models, two benchmark problems are considered and LBM results are compared with the analytical solutions. The dendrite growth model was previously validated and compared with other simulation results. More details on the dendrite growth model validation can be found in Chapter III and Reference [6].

4.3.1.1 Fluid flow

For fluid flow validation, a benchmark problem of a steady state laminar flow over a circular cylinder that is asymmetrically placed inside a channel is considered. Schäfer and Turek [8] reported a set of results obtained from several different numerical methods for this case. They also presented the estimated intervals for the “exact” results

on the basis of the obtained solutions. An identical geometry with the same initial and boundary conditions is employed to reproduce the benchmark results reported by Schäfer and Turek [8].

Figure 4.2 shows the configuration and boundary conditions for flow around a circular cylinder. The inflow condition is $U(0, y, z) = 16U_m yz(H - y)(H - z)/H^4$, $V = W = 0$ with $U_m = 0.45$ m/s. For no slip boundary condition on the walls and the cylinder, the bounce-back rule is used. The inflow condition is imposed by specifying the given velocity profile at the entrance, and a zeroth-order extrapolation for the distribution function is imposed at the exit. Density and viscosity are assumed to be 1 kg/m^3 , and $0.001 \text{ m}^2/\text{s}$, respectively. The method suggested by Mei et al. [9] is used to calculate drag and lift forces, and consequently drag and lift coefficients, as well as pressure drop. Table 4.1 shows the LBM results for three different meshes. The last two rows present the intervals of the exact solution as reported by Schäfer and Turek [8]. It is observed that the error in the drag and lift coefficients is larger for coarser grids. The reason is that the discretization of the nodes using a rectangular mesh cannot precisely reproduce the circular outline of the cylinder. However, the pressure drop across the cylinder is inside the bound for all three meshes used. It should be noted that the mesh size employed for dendrite growth simulations is much smaller than the finest mesh used for fluid flow validation.

Table 4.1 Fluid characteristic quantities for steady state laminar flow over a cylinder. Simulation results are listed for three different node spacings. Lower and upper bounds present the estimated interval for the exact results [8].

Node Spacing (m)	c_d	c_l	ΔP
0.005	6.6315	0.0225	0.1730
0.0025	6.3503	0.0148	0.1702
0.00166	6.2550	0.0082	0.1681
Lower Bound	6.0500	0.0080	0.1650
Upper Bound	6.2500	0.0100	0.1750

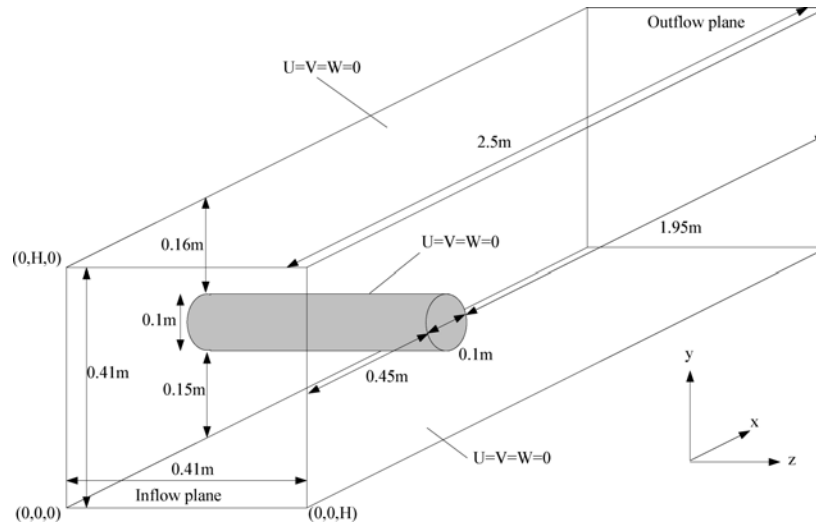


Figure 4.2 Configuration and boundary conditions for the benchmark problem of steady state laminar flow over a cylinder [8].

4.3.1.2 Solute transport

For the one-dimensional case of an instantaneous volume source of mass over the range $-\infty < x < 0$ with concentration C_i , and for a steady velocity field $\mathbf{u} = (U_0, 0, 0)$, the solution of the diffusion-advection equation is given by [10]:

$$\frac{C(x,t)}{C_i} = \frac{1}{2} \left(1 - \operatorname{erf} \left(\frac{x-U_0 t}{\sqrt{4Dt}} \right) \right) \quad (4.14)$$

This case is examined for a 3D channel with a square cross section. A one-dimensional flow of $U_0=10$ mm/s, enters the domain from the left wall and exits through the right wall. Periodic boundary conditions are applied to the side walls. The concentration of the source is considered to be $C_i = 4$ wt%. Figure 4.3 shows the concentration profile in the x-direction after 2 ms. The channel is long enough and the considered time is short enough, so that the concentration remains unchanged at regions close to right and left boundaries and the infinity assumption is correct. A good agreement is found between LB and analytical solutions.

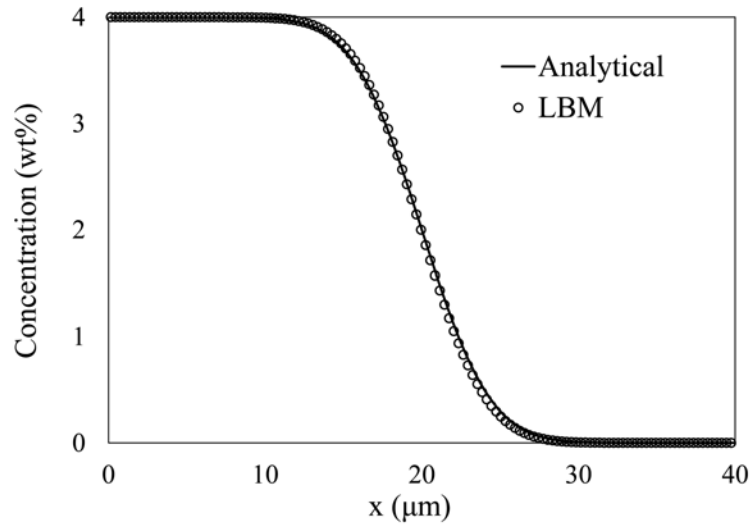


Figure 4.3 Comparison between the solute distribution calculated using LB and analytical models for diffusion-advection under $U_0=10$ mm/s after 2 ms.

4.3.2 Dendrite growth under melt convection

In this section, the simulation results for dendritic growth under melt convection are discussed. The growth features are compared for 2D and 3D simulations. In addition, the impact of altering melt undercooling, inlet flow velocity, and alloy composition on the kinetics of 3D dendrite growth is explored.

4.3.2.1 Kinetics of growth under forced convection

Figure 4.4 depicts the evolution of dendritic morphologies after 2, 4, 6, and 8 ms under the effect of melt convection. A uniform flow with inlet velocity $U_0=7$ mm/s enters the domain from the left face. The fluid convection affects the solute distribution around the dendrites and consequently alters the kinetics of dendritic growth. The cubic simulation domain contains 288^3 cubic cells with $\Delta x=0.3$ μm . The domain is uniformly cooled down up to 4.5 $^{\circ}\text{C}$ below the melting point ($\Delta T=4.5$ $^{\circ}\text{C}$). The streamlines show how flow travels around the growing dendrite. Moreover, the morphology of the dendrite in 2D sections perpendicular to z-direction and passing through the dendrite center is shown in Figure 5.5. The wireframes show the morphologies, from inside to outside, respectively after 0.75, 2.00, 3.25, 4.50, 5.75, 7.00, 8.25, and 9.00 ms. At the initial stages of solidification, the primary arms grow along their crystallographic orientation without any secondary arms. As solidification proceeds, the primary arms grow and coarsen, and then, the secondary arms start to grow perpendicular to the primary arms. Melt convection washes the solute from upstream primary and secondary arms and transports it downstream. This leads to a lower concentration in the upstream area and a higher concentration downstream and consequently, a higher growth rate upstream and a lower growth rate downstream. This matches the findings of previous studies [1, 4, 5, 11,

12, 13]. Although the transverse arms (the ones in the y and z directions) are not significantly affected by convection, the secondary branches grow faster on the upstream side of the transverse arms.

Figure 4.6 shows the melt flow around the dendrite. Velocity values are higher in the areas far from the dendrite and lower in the dendrite's vicinity. The bottom part of Figure 4.6 shows the solute concentration in two perpendicular planes passing through the center of the dendrite. As solidification advances, since the solubility of solute in solid is less than its solubility in liquid, the extra solute is rejected to the interface. At later times, when solidification is close to completion, there are liquid regions encompassed by the solid phase, holding a high concentration. Those regions may end up causing micro-segregation or forming eutectic phases.

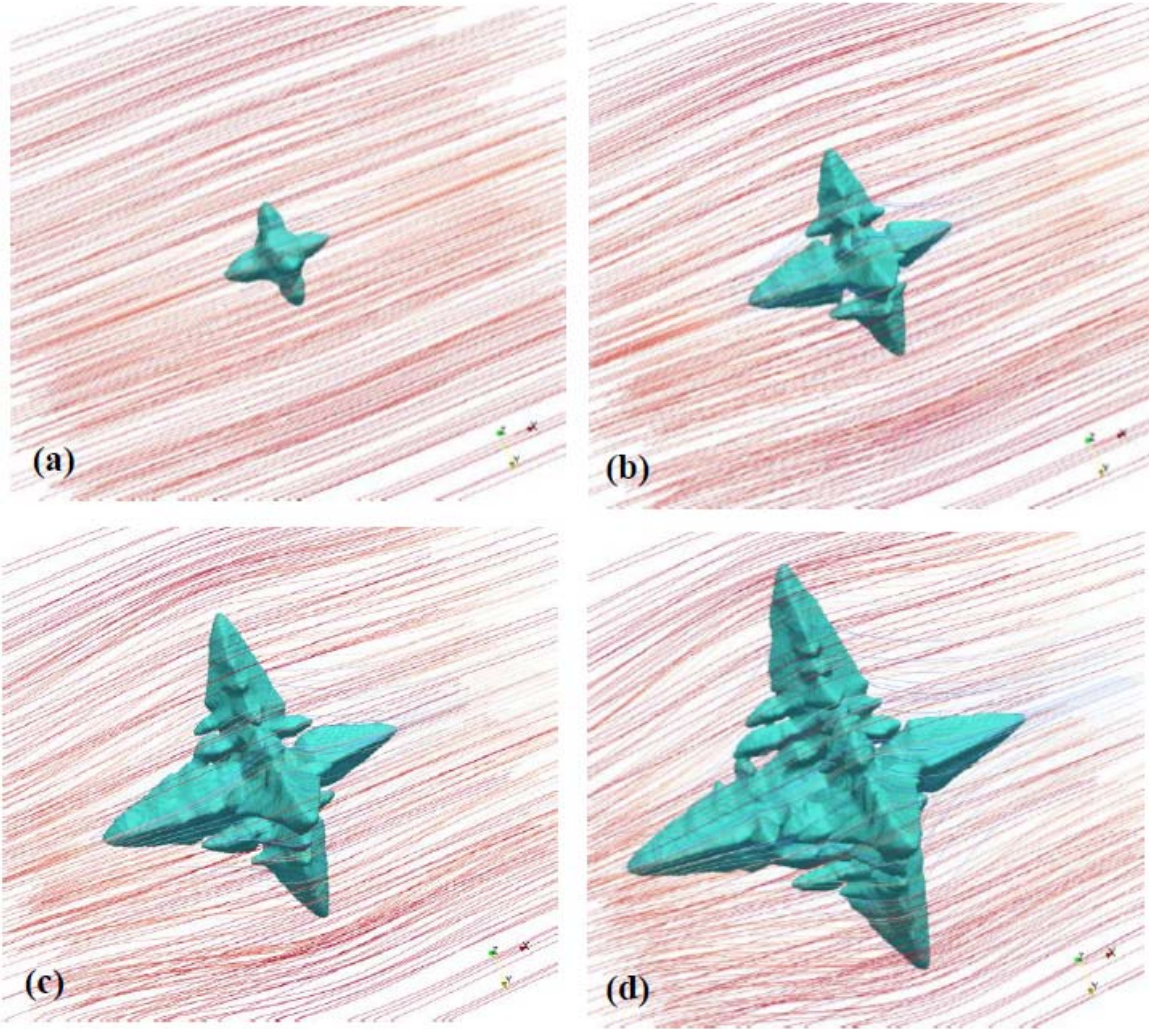


Figure 4.4 Evolution of dendritic structures under melt convection after (a) 2, (b) 4, (c) 6, and (d) 8 ms.

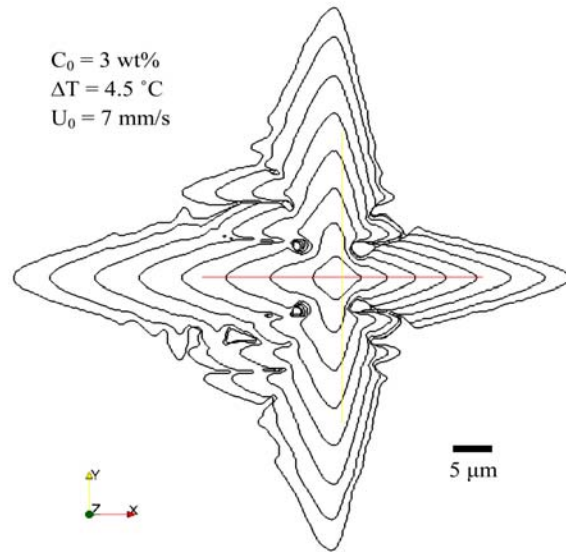


Figure 4.5 2D sections showing the morphological changes of the 3D dendrite growing under melt convection.

From the innermost frame to the outermost frame, after 0.75, 2.00, 3.25, 4.50, 5.75, 7.00, 8.25, and 9.00 ms, respectively.

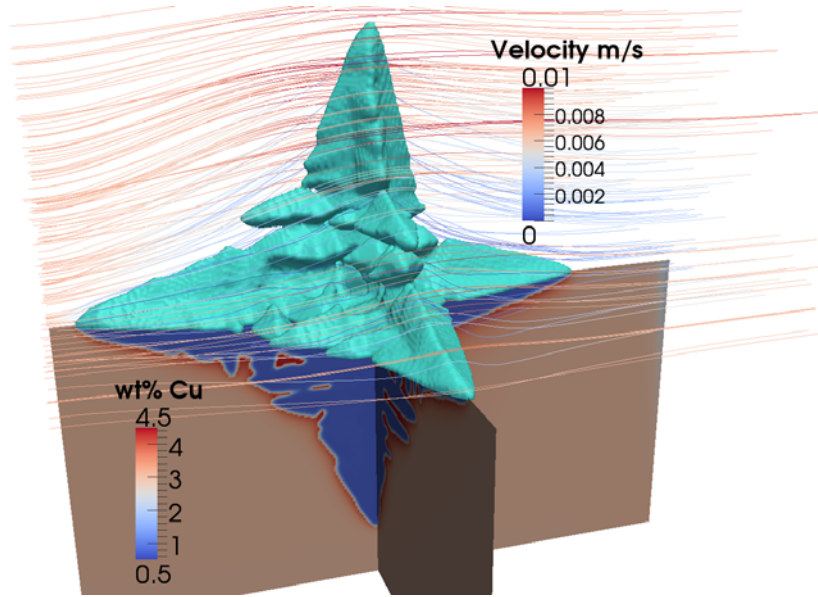


Figure 4.6 Snapshot of a 3D solutal dendrite growing under melt convection.

The top part depicts the 3D dendrite morphology with the streamlines showing the melt velocity around it. The bottom part shows the solute distribution in two perpendicular cross sections.

4.3.2.2 Comparison of 2D and 3D simulations

As mentioned before, studies have shown that the kinetics of dendrite growth is considerably different in two and three dimensions. Even when convection is not present, diffusion is more effective in 3D compared to 2D. Therefore, solute concentration and its gradient are higher around 2D dendrites, causing a slower growth. Figure 4.7 compares the solute distributions in 2D and 3D domains. The results are captured after an identical time of 7.5 ms for both cases. 2D simulations are performed with a similar methodology as 3D, but using the D2Q9 lattice. Interested reader is referred to Reference [13] for more details on the 2D model. Fluid convection affects the solute distribution around the dendrites and consequently alters the kinetics of dendritic growth. Melt flow results in a thinner solute layer around the 3D dendrite in comparison with the 2D dendrite and thus a

higher tip velocity, something that is also confirmed by other studies [5]. This effect restrains the side branches to form in 2D, but promotes their growth in 3D, especially upstream. Comparison of 2D and 3D sections reveals that the center of the 3D dendrite is somewhat displaced towards the upstream direction under the effect of convection, something that is not detected in 2D results, as 2D flow cannot sweep the solute downstream as effectively as in 3D. This displacement can also be observed in the results obtained from phase field simulations [1, 14].

Figure 4.8 depicts the x-component of velocity around 2D and 3D dendrites. Note that the color legends are different for 2D and 3D cases. While melt can flow around the dendrites in 3D simulations, melt flow is blocked by the 2D dendrite and cannot go around the arms. As a result, the maximum velocity is much higher in the 2D domain compared to 3D. It can be seen that the downstream side of the 2D dendrite faces much less convection than the 3D one, hence more solute accumulation and less growth. There is no apparent recirculation downstream the 3D dendrite because liquid can flow more freely around the dendrite while recirculation past the dendrite is very likely in 2D. These effects altogether cause a more significant difference between the arms growing in upstream and downstream directions in a 2D domain. The length ratio of the upstream arm to the downstream arm in Figure 4.8 is 2.75 for the 2D case, while it is 1.43 for the 3D case. The results of the simulations indicate that the length ratio increases with time for both cases.

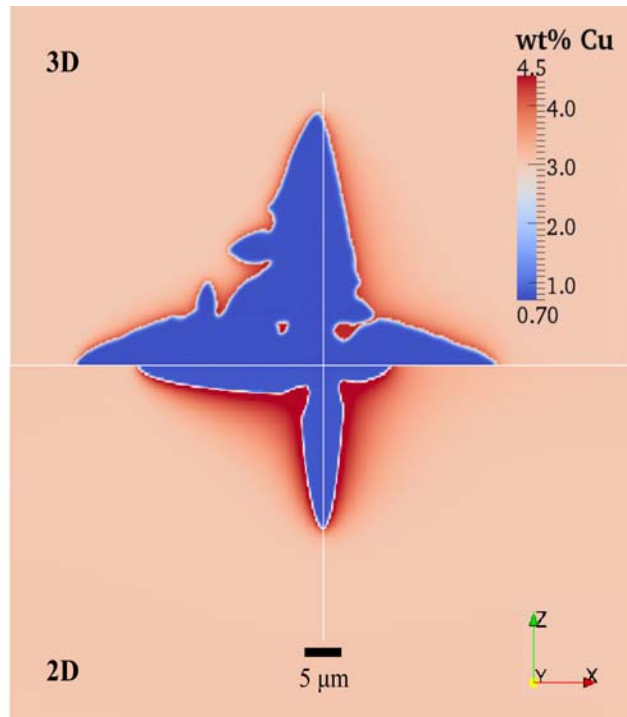


Figure 4.7 Solute distribution around 2D and 3D dendrites.

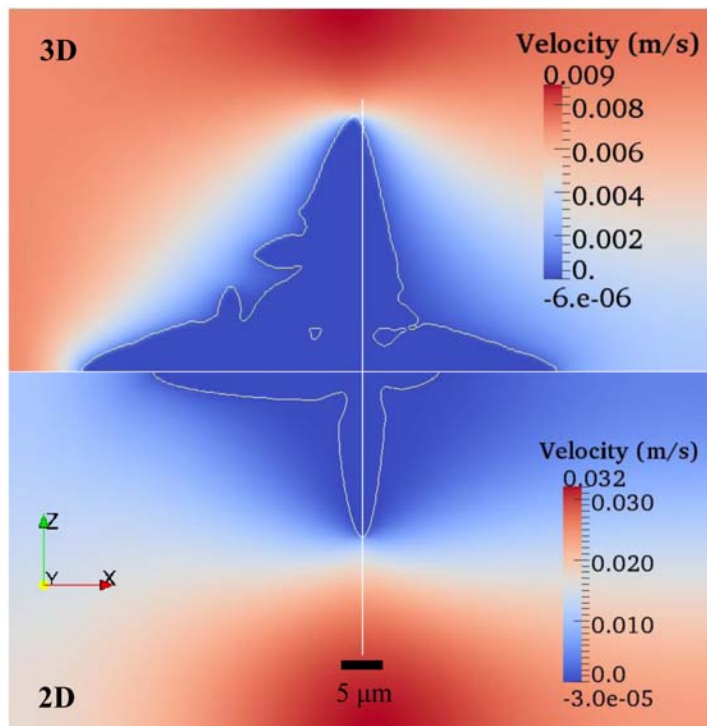


Figure 4.8 Contours showing the x-component of velocity around 2D and 3D dendrites.

4.3.2.3 Effect of melt undercooling

Figure 4.9 shows the variation of tip velocity with undercooling. All simulations are performed for Al-3wt%Cu alloy with an identical inlet velocity, $U_0=7$ mm/s, as in the previous section. The growth rate and tip velocity increase with undercooling for all branches. Upstream tip velocity is the highest whereas downstream tip velocity is the lowest and the tip velocity of the transverse arms is in between. The melt flow washes the solute atoms from the upstream tip, reducing the local concentration in front of the tip. Thus, the difference between the local and equilibrium solute concentrations increases and leads to a faster growth. On the other hand, melt convection causes an increase in the solute concentration in front of the downstream tip and consequently decreases the growth rate. Fluid flow has no substantial impact on the solute concentration at the tip of the transverse arms, because the fluid flow does not produce a solutal gradient in the transverse tip growth direction as done with the upstream arm tip. It can be seen that the average tip velocity of the transverse arms is almost same as the tip velocity for the case without fluid flow.

Figure 4.10 shows 2D sections of the 3D dendrite growing in melts with different undercoolings. The bottom and top halves present morphologies of the dendrite growing in the melt with 3 and 4 °C of undercooling, respectively. Different colors represent different times. As expected, the dendrite growing in the melt with $\Delta T=4$ °C grows faster compared to the dendrite growing in the melt with $\Delta T=3$ °C. However, the impact of melt convection is more significant for the dendrite with smaller undercooling, because convection has more time to accumulate solute downstream. The difference between the lengths of upstream and downstream branches is bigger for the smaller undercooling. The

difference increases with time, as the downstream arm grows very slowly for $\Delta T = 3^\circ\text{C}$. As a result of faster growth, secondary branches also form sooner in the melt with larger undercooling.

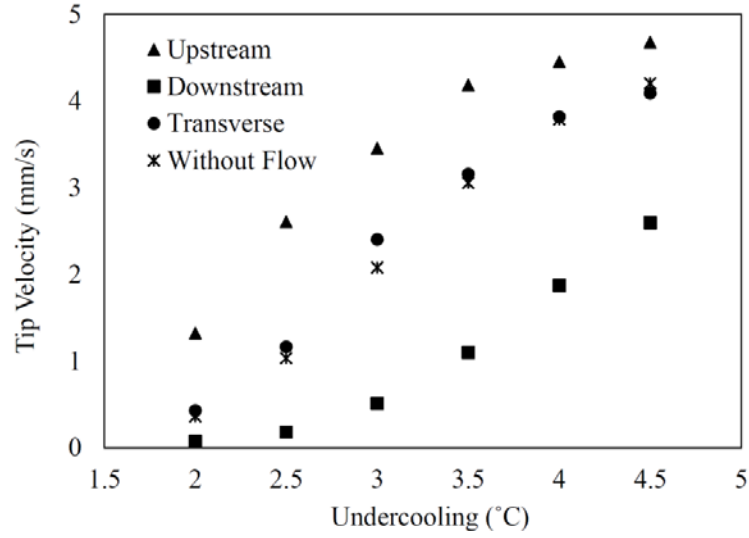


Figure 4.9 Variation of average tip velocity with undercooling for upstream, downstream, and transverse branches of a dendrite growing under inlet velocity of $U_0 = 7$ mm/s and the case without melt convection.

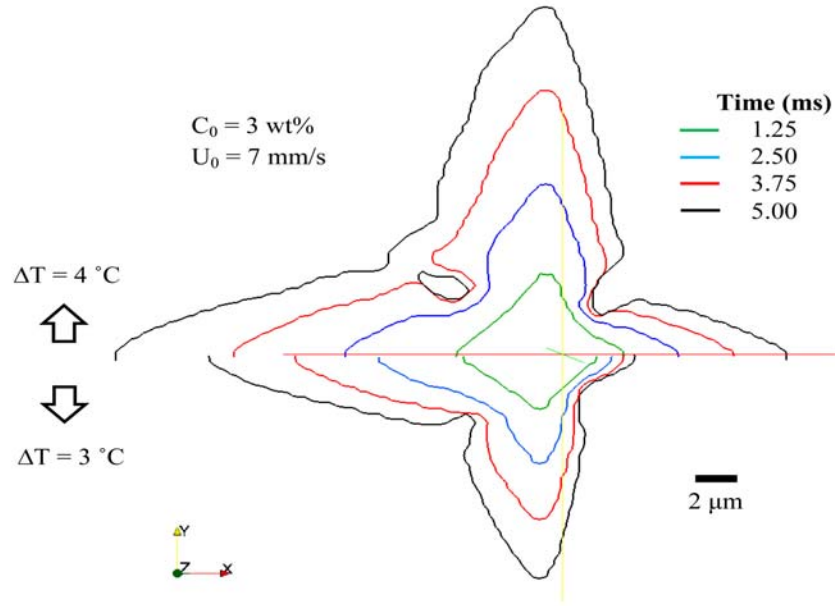


Figure 4.10 Comparison of dendritic morphologies growing in melts with different degrees of undercooling: top: $\Delta T = 4\text{ }^{\circ}\text{C}$, and bottom: $\Delta T = 3\text{ }^{\circ}\text{C}$.

Different colors represent different times.

4.3.2.4 Effect of inlet velocity

Variation of tip velocities with inlet flow velocity is shown in Figure 4.11. The solute concentration and undercooling are considered to be 3 wt% and $4.5\text{ }^{\circ}\text{C}$, respectively. Increasing flow velocity slightly increases the growth velocity of the upstream arm. As mentioned before, fluid flow does not seem to have a significant effect on the transverse arms. Even for high inlet velocities, the transverse arms don't seem to be much affected. Increasing flow velocity shows a more significant effect on the tip velocity of the downstream arm. By increasing the flow velocity, more solute is accumulated around the downstream arm, increasing the local liquid composition. The change in the fraction of solid is reduced as the local liquid composition increases, which results in a lower growth rate. A tip splitting phenomenon is observed for inlet velocities

higher than 10 mm/s, leading to inaccurate and unstable measurement of the tip velocities.

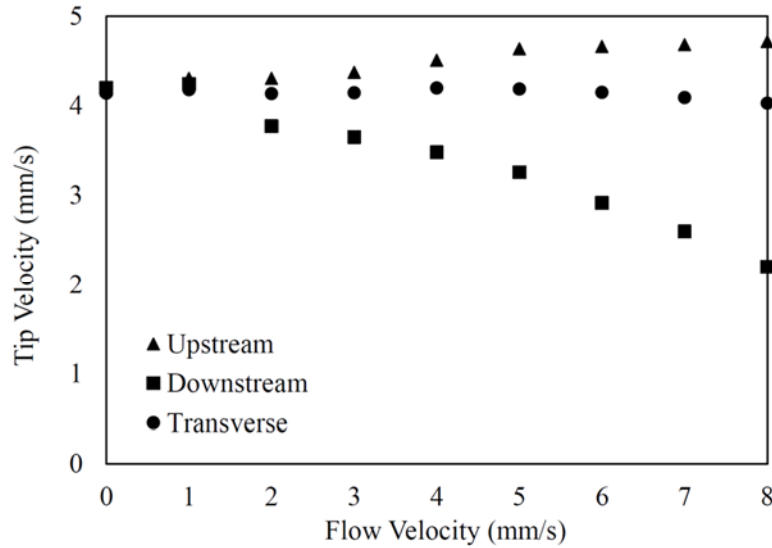


Figure 4.11 Variation of average tip velocity with inlet melt velocity for Al-3wt%Cu alloy with $\Delta T=4.5$ °C.

Figure 4.12 illustrates the morphologies of the dendrites growing under different flow velocities. As the inlet velocity increases, the dendrite grows faster in the direction opposite to the flow direction. Increasing flow velocity does not show a significant impact on the length of the upstream arm. Interestingly, the flow washing away the solute layer at the interface causes enhanced growth on all the upstream faces of the dendrite, producing a net displacement of the dendrite center towards the upstream direction. This displacement increases with the magnitude of the inlet velocity. It can be seen that the distance from the center of the simulation domain to the dendrite's tip is slightly longer, but there is not much difference between the distance from the center of dendrite to the

upstream tip for dendrites growing under different flow velocities. As mentioned above, increasing the flow velocity has a more significant influence on the downstream arm. Flow velocity slightly decreases the tip velocity of the transverse arms, but the effect is not considerable. However, as inlet velocity increases, growth of secondary arms on the transverse arms is promoted in the upstream direction.

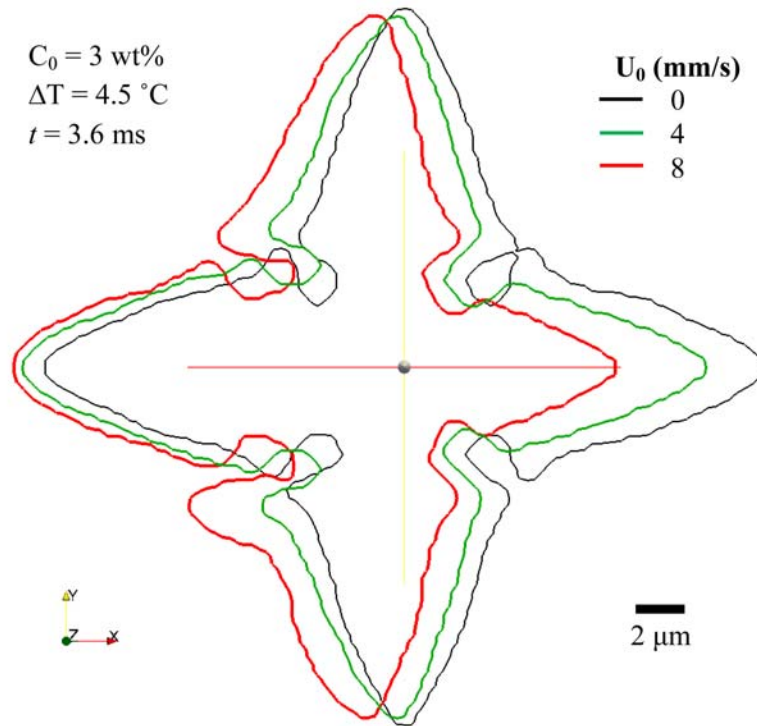


Figure 4.12 Effect of inlet velocity on the morphology of Al-3wt%Cu dendrites. Different colors represent different inlet velocities: 0, 4, and 8 mm/s.

4.3.2.5 Effect of alloy composition

Effect of alloy composition on the growth kinetics is displayed in Figure 4.13. The undercooling and inlet velocity are identical for all cases and considered to be 4.5 $^\circ\text{C}$ and 7 mm/s, respectively. In general, the growth rate decelerates with increasing

concentration of the solute. As the alloy's solute content increases, all upstream, downstream, and transverse tip velocities decrease with a comparable rate. This is an expected trend due to the constant partition coefficient and liquidus slope used in the simulations.

Figure 4.14 depicts 2D wireframes of the 3D dendrites growing in melts with different compositions. The bottom and top sections represent Al-3wt%Cu and Al-9wt%Cu alloys, respectively and the colors indicate different times. Note that since the growth rates are significantly different, showing the outlines at identical times for both compositions may not illustrate the detail of dendritic morphologies. The only time at which the morphology is displayed for both compositions is $t = 3.5$ ms that is presented by red in Figure 4.14. As can be seen, the growth speed is considerably faster in the alloy with lower solute concentration. In addition, the size ratio of the upstream arm to the downstream arm is significantly bigger in the alloy with higher solute concentration. Because the dendrite grows very slowly in Al-9wt%Cu alloy, convection can effectively wash the solute from upstream and accumulate it downstream. Hence, the local liquid concentration stays always high in front of the downstream arm, hindering the arm's advancement and increasing the length ratio between upstream and downstream arms.

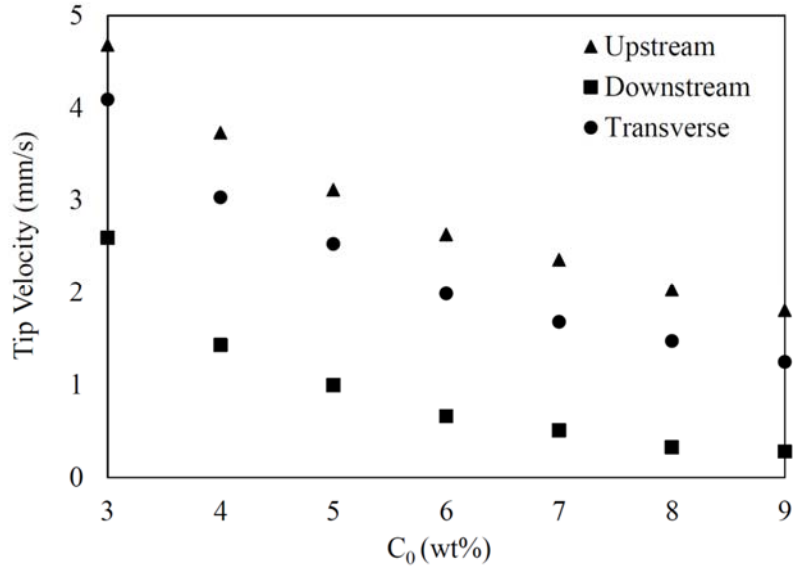


Figure 4.13 Variation of average tip velocity with initial alloy composition under $U_0=7$ mm/s, and $\Delta T=4.5$ °C.

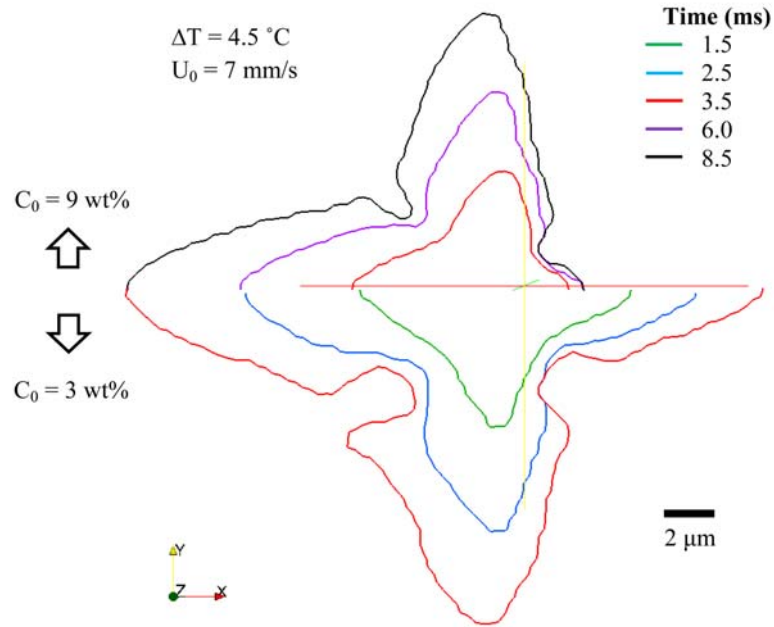


Figure 4.14 Effect of alloy composition on the dendritic morphology under inlet velocity of $U_0=7$ mm/s, and $\Delta T=4.5$ °C.

Top: Al-9wt%Cu, and bottom: Al-3wt%Cu. Different colors represent different times.

4.4 Conclusions

A three-dimensional lattice Boltzmann model is introduced for simulating dendritic growth under forced convection. The results show that growth kinetics and dendritic morphology are significantly affected by the presence of fluid flow. The primary and secondary arms grow faster in the upstream direction, and significantly slower in the downstream direction. The fluid flow does not show a noticeable impact on the transverse arms and the tip velocity in those directions is similar to the case without convection. A comparison with 2D results revealed that 3D dendrites grow faster in general, but the difference between the velocity of upstream and downstream arms is more significant in 2D simulations. Moreover, 3D dendrites seem to be more likely to form side branches. It was found that the center of the 3D dendrite is slightly displaced upstream under the influence of melt convection. The displacement increases with inlet velocity. Increasing the degree of undercooling accelerates the growth rate in all directions. By increasing the magnitude of flow velocity, the convection effects are intensified. The influence on the downstream arm seems more significant in comparison with the upstream arm. The growth rate slows down in all branches when the alloy contains a higher solute concentration. The size ratio of the upstream arm to the downstream arm grows by increasing inlet velocity and solute content, and decreasing undercooling. Considering the special capabilities of the lattice Boltzmann method, e.g. simple implementation, computational efficiency, local calculations, and inherent parallel structure; the model offers a great potential for simulating the solidification of 3D dendritic structures under convection.

The results of this chapter are partially presented in the 2013 TMS Annual Meeting & Exhibition. In addition, a journal manuscript was prepared from the content of this chapter and is under review for publication.

4.5 References

- [1] J-H. Jeong, N. Goldenfeld, J. A. Dantzig, Phase field model for three-dimensional dendritic growth with fluid flow, *Physical Review E* 65 (2001) 041602.
- [2] J-H. Jeong, J. A. Dantzig, N. Goldenfeld, Dendritic growth with a fluid flow in pure materials, *Metallurgical and Materials Transactions A* 34 (2003) 459-466.
- [3] A. Karma, W. J. Rappel, Phase-field simulation of three-dimensional dendrites: is solvability theory correct?, *Journal of Crystal Growth* 174 (1997) 54-64.
- [4] Y. Lu, C. Beckermann, J. C. Ramirez, Three-dimensional phase-field simulations of the effect of convection on free dendritic growth, *Journal of Crystal Growth* 280 (2005) 320-334.
- [5] L. Yuan, P. D. Lee, Numerical Simulations on Dendritic Solidification under Forced and Natural Convection for Binary Alloys: 2D vs. 3D, *Modelling and Simulation in Materials Science and Engineering* 18 (2010) 055008.
- [6] M. Eshraghi, S. D. Felicelli, B. Jelinek, Three dimensional simulation of solutal dendrite growth using lattice Boltzmann and cellular automaton methods, *Journal of Crystal Growth* 354 (2012) 129–134.
- [7] J. Bhatnagar, E. P. Gross, M. K. Krook, A model for collision processes in gases: I. Small amplitude processes in charged and neutral one-component system, *Physical Review* 94 (1954) 511–525.
- [8] M. Schäfer, S. Turek, Benchmark computations of laminar flow around a cylinder, *Flow Simulation with High-Performance Computers II, Notes in Numerical Fluid Mechanics* ed E H Hirschel EH (Vieweg, Braunschweig, Germany) 52 (1996) 547.
- [9] R. Mei, D. Yu, W. Shyy, L-S. Lou, Force evaluation in the lattice Boltzmann method involving curved geometry, *Physical Review E* 65 (2002) 041203.
- [10] S. A. Socolofsky, G. H. Jirka, Special topics in mixing and transport processes in the environment, *Engineering–Lectures* 5th ed. (College Station (TX): Coastal and Ocean Engineering Division, Texas A&M University) (2005).
- [11] Y. Lu, C. Beckermann, A. Karma, Convective effects in three-dimensional dendritic. *Materials Research Society Symposium Proceedings* 701 (2002) T2.2.1-10.
- [12] D. Sun, M. F. Zhu, S. Pan, D. Raabe, Lattice Boltzmann modeling of dendritic growth in a forced melt convection, *Acta Materialia* 57 (2009) 1755–1767.

- [13] H. Yin, S. D. Felicelli, L. Wang, Simulation of dendritic microstructure with lattice Boltzmann and cellular automaton methods, *Acta Materialia* 59 (2011) 3124–3136.
- [14] C. C. Chen, Y. L. Tsai, C. W. Lan, Adaptive phase field simulation of dendritic growth in a forced flow: 2D vs 3D morphologies, *International Journal of Heat Mass Transfer* 52 (2009) 1158-1166.
- [15] M. Eshraghi, B. Jelinek, S. D. Felicelli, A three-dimensional lattice Boltzmann-cellular automaton model for dendritic solidification under convection, 2013 TMS Annual Meeting & Exhibition, San Antonio, TX (2013).

CHAPTER V

LARGE-SCALE SIMULATION OF DENDRITIC SOLIDIFICATION

5.1 Introduction

Despite the current advances in the large scale parallel supercomputing, only a handful of studies of large-size solidification domains have been performed. Parallel simulations of 3D dendrite growth have been performed utilizing the phase field method [1]. Improved, multigrid phase field schemes presented by Guo et al. [2] allow parallel simulations of tens of complex shape 2D dendrites in a simulation domain of up to $25\text{ }\mu\text{m} \times 25\text{ }\mu\text{m}$ size. Shimokawabe et al. [3] deployed a modern heterogeneous GPU/CPU architecture to perform the first peta-scale 3D solidification simulations. However, none of these models included convection.

In this chapter, large scale simulations of dendrite growth using a parallel LB-CA model are presented. The parallel implementation and performance of the model is also discussed.

5.2 Parallelization

The algorithm is parallelized using MPI technique with spatial domain decomposition. The global rectangular grid is split into equally sized subregions, and each computational core allocates the data and performs computation in only one

subregion. Given the convenient locality of the LB-CA model, only the values on the subdomain boundaries need to be exchanged between subdomains.

The LBM performs a sequence of streaming and collision steps. Collision calculates new value of the distribution function. The collision step is completely local and does not require values from the surrounding cells. Each execution core has the data it needs available, and no data exchange with neighboring subdomains is required. The other step, assignment operation in the equation, is referred to as streaming. Streaming step involves propagation of each distribution function to the neighboring cells. Except for the stationary f_0 , each distribution function f_i is propagated in the direction of the corresponding lattice velocity e_i ($i = 1 \dots 15$, for D3Q15 lattice). For the neighboring cells belonging to the computational subdomain of another execution core, the distribution functions are transferred to the neighboring subdomains using MPI communication routines. During the streaming step, permanent storage is allocated only for values from the local subdomain. When the streaming step is due, temporary buffers are allocated to store the data to be sent to (or received from) other execution cores.

When calculation in a particular lattice cell needs values from the neighboring cells, the neighboring cells may belong to the computational subdomains of other execution cores. Therefore, the values needed may not be readily available to the current execution. To provide access to the data from other executions, an extra layer of lattice sites is introduced at the boundary with each neighboring subdomain. Values from these extra boundary layers, referred to as ghost layers, are populated from the neighboring subdomains. Population of the ghost sites is a common operation in parallel stencil codes.

Figure 5.1 shows the communications involved in a 2D slice when the ghost sites are populated for the execution core 5.

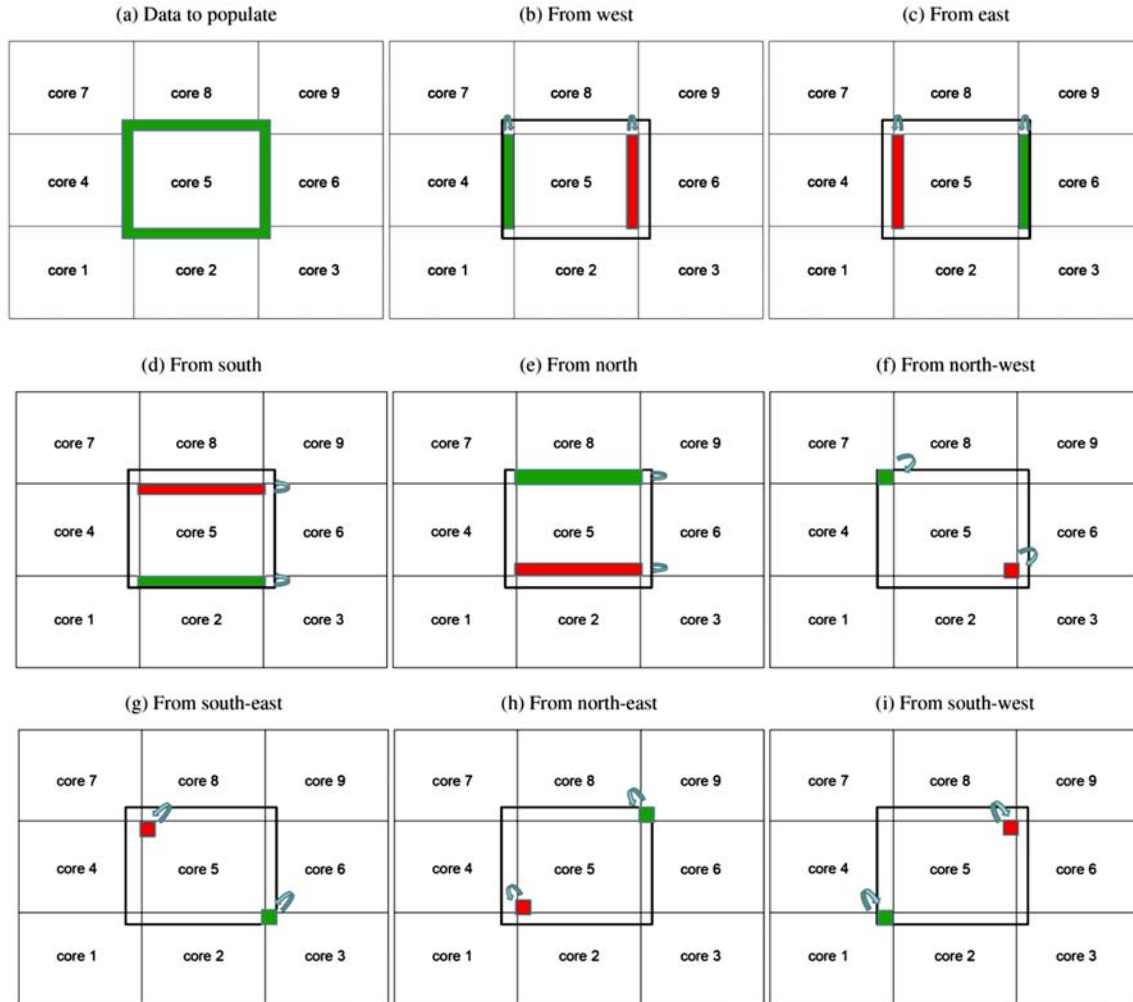


Figure 5.1 Populating the ghost values (green area in part (a)) on the execution core 5. Each subdomain permanently stores an extra “ghost” layer of values to be received from (or to be sent to) the neighboring subdomains. Synchronously with receiving the data, the execution core 5 sends the data in the direction opposite to where the data is received from.

Throughout the solidification process, the solute is rejected from the interface and redistributed from the solidifying cells to the neighboring cells. In this case, the ghost

layers are used to store the amount of solute to be distributed to the neighboring subdomains.

As the size of the simulation domain increases, the storage, processing, and visualization of results requires more resources. The parallel writing of simulation variables is implemented in a binary HDF5 format [4]. Publicly available HDF5 library eliminates the need to implement low level MPI I/O routines. Data stored in the standard HDF5 format is straightforward to visualize using common visualization tools. In the binary format, the data is stored without a loss in accuracy.

5.3 Parallel performance

As previously mentioned, locality and intrinsic parallel structure are among the most important features of LB and CA methods. Kraken, located at the Oak Ridge National Laboratory, was used to perform the parallel performance tests. Kraken is a Cray XT5 system with 9,408 total computing nodes, each with 16 GB of memory and two six-core AMD Opteron “Istanbul” processors (2.6 GHz), connected by Cray SeaStar2+ router.

5.3.1 Strong scaling

To characterize the gain from parallelization, one can compare the calculation time of the task of a certain size on one execution core with the calculation time on multiple cores, referred to as the strong scaling. Ideally, when running on n cores, the computation is expected to be n times faster which means 100% parallel efficiency. Intuitively, the speed up is defined as the ratio of the computation time on a single core to the computational time using n cores.

Figure 5.2 shows the speed-up performance of the code. For the speed up tests, the domain was equally divided and the computational load was equally distributed among the computational cores. Nearly excellent speed up is demonstrated, with only slight degradation in parallel performance when more than 1000 computation cores are deployed. The smallest number of cores was 16 for the simulations. Ideal performance is expected when the tasks solved by individual cores are independent. When the tasks to be solved by individual cores depend on each other, the efficiency usually decreases with the number of cores. As the communication cost becomes comparable with computation cost, the efficiency goes down. Due to the high memory bandwidth requirement of the algorithm, an increase in the utilized number of cores in one node causes parallel performance loss. On the contrary, when two cores per node are used, the parallel efficiency remains close to the ideal performance for high number of cores.

5.3.2 Weak scaling

Increasing the number of the execution cores and the associated memory allows solving problems in larger domains. If the number of cores is multiplied by n , and the simulation domain also increases by the factor of n , the simulation time should not change. This, so called weak scaling of the algorithm, is characterized by the scale up efficiency. However, the scale-up performance degrades by increasing the number of processors/subdomains, due to the rise in the cost of communications. For scale up tests, the domain was periodically duplicated along three dimensions. The calculation time is shown in Figure 5.3. An excellent, virtually ideal scale up is observed. The code shows a slight degradation in the scale up performance when large number of cores is employed.

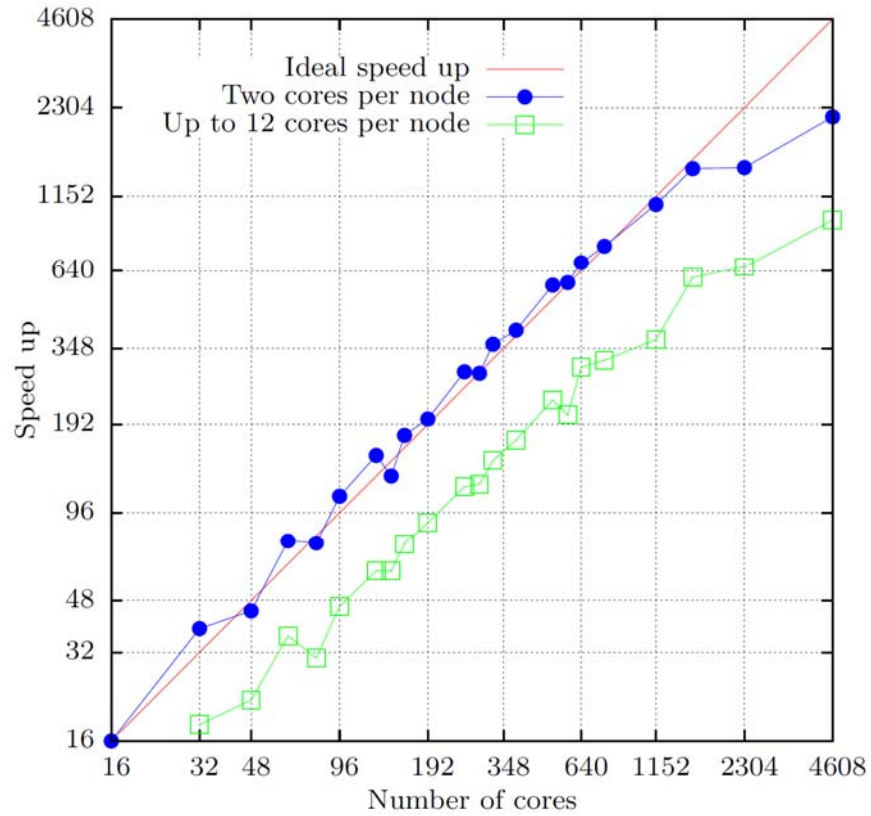


Figure 5.2 Speed up performance (increasing number of processors with a fixed domain size).

5.4 Large scale columnar growth

At the beginning of simulation, a number of solid seeds with random positions and crystallographic orientations are placed at the bottom of a domain of the undercooled molten alloy. This is similar to what is observed in many industrial applications, where alloys are directionally solidified in conditions that produce a complex array of columnar dendrites.

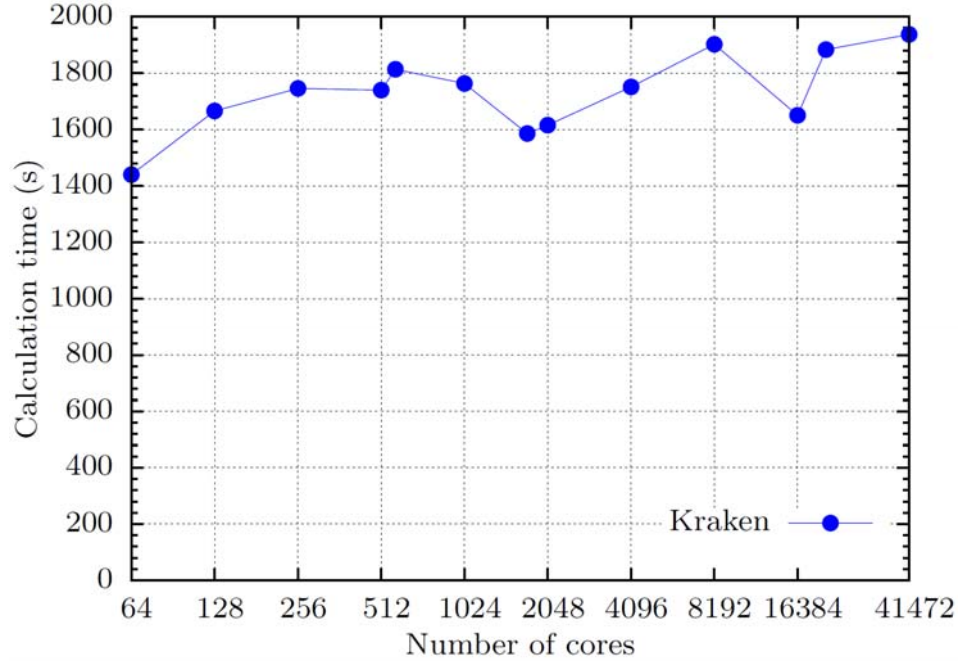


Figure 5.3 Scale up performance (fixed processor load by scaling the domain size). The calculation time at each point is relative to the calculation time when the smallest number of cores was deployed.

Figure 5.4 displays the simulation results of the columnar dendritic growth in the melt of Al-3wt.%Cu alloy with 4.5 °C undercooling. The domain dimension is $720 \times 720 \times 720$ which is equivalent to $216 \times 216 \times 216 (\mu\text{m})^3$. Two different views, parallel and perpendicular to the growth direction, are presented. Columnar dendrites growing in different orientations with well-developed side branches can be observed in the pictures, which are very similar to the morphologies observed in the experimental micrographs. Dendrites compete with each other and the ones with orientations other than 90 degrees are blocked by the perpendicular dendrites. So, the dendrites that survive to grow to the top are all parallel to each other. The flat tips or sides observed in some cases are due to the dendrites touching the domain boundaries.

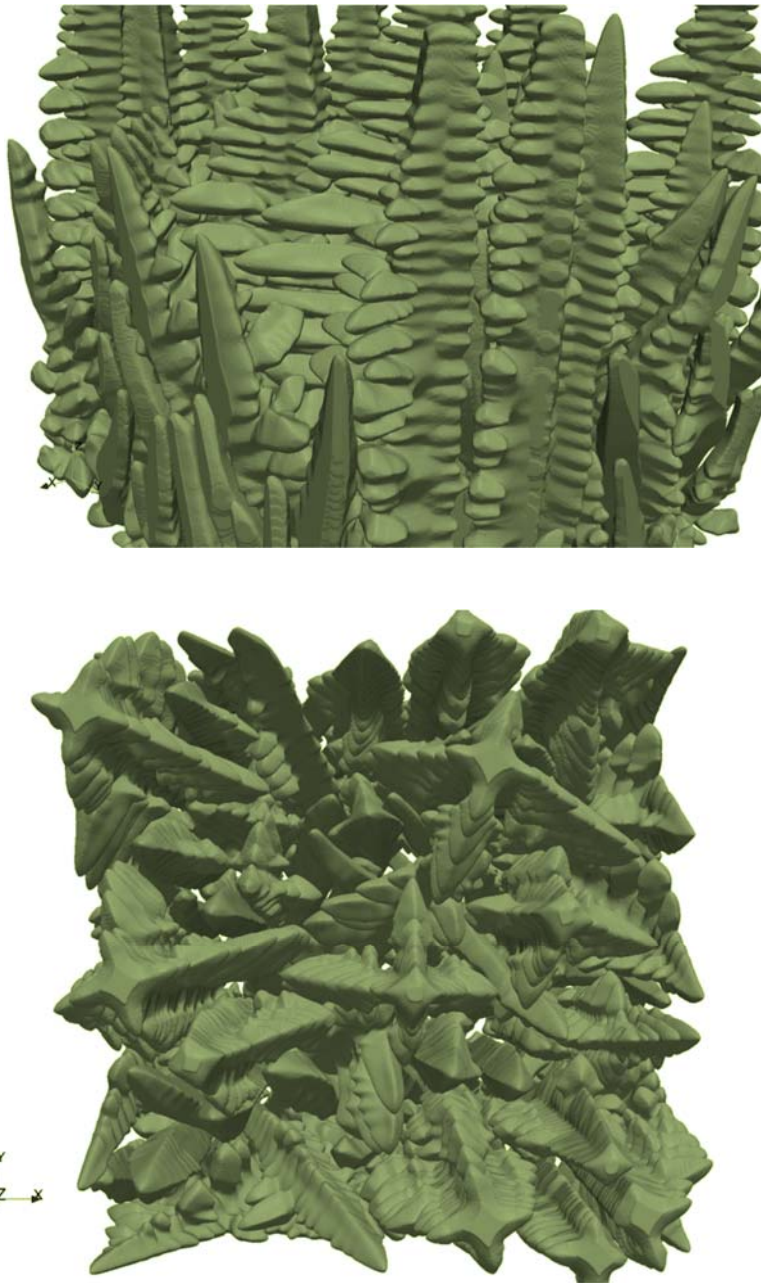


Figure 5.4 Columnar dendrites growing in an undercooled melt of the Al-3wt.%Cu alloy.

Figure 5.5 shows the solute distribution around the 3D columnar dendrites illustrated in Figure 5.4. The legend shows the weight percent of copper. During the

solidification, since the solubility of solute in solid is less than its solubility in liquid, the extra solute is rejected to the interface resulting in the higher solute copper concentration between the dendritic arms. At later stages of solidification, the high concentration regions may cause micro-segregation or form eutectic phases.

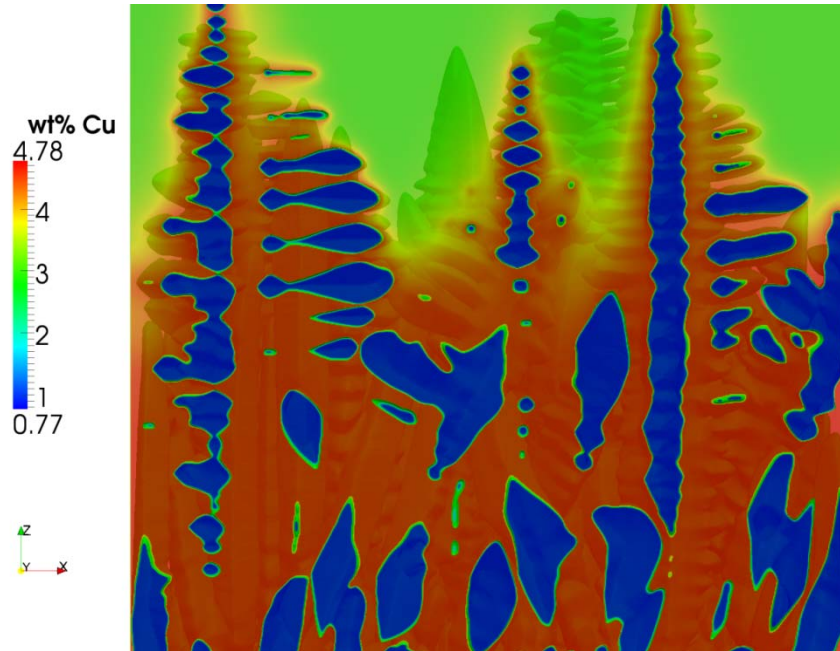


Figure 5.5 Solute distribution around 3D columnar dendrites.

The domain contains $600 \times 600 \times 480$ 3D cubic lattices that corresponds to a physical domain of $180 \times 180 \times 144 \text{ } (\mu\text{m})^3$.

Figure 5.6 shows a 3D domain with the size of $3300 \times 3300 \times 3300$ grid cells; around 36 billion grid points in total. With the mesh size of $\Delta x = 0.3 \text{ } \mu\text{m}$, this domain represents a volume close to 1 mm^3 . To the author's knowledge, such large domain has never been presented in any literature before and this is the largest dendrite growth simulation performed to date. Around 4000 seeds with random positions and

crystallographic orientations were initially distributed at the bottom of the domain. The dendrites grow in the undercooled melt and then develop side branches. Again, the tilted dendrites are blocked by the dendrites growing in perpendicular directions.

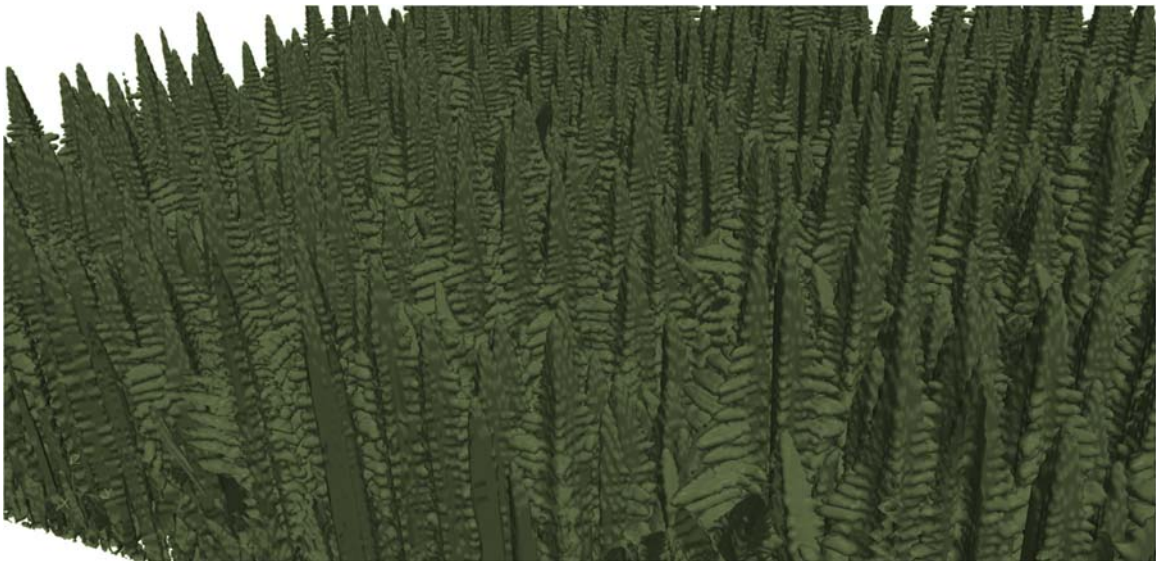


Figure 5.6 Large scale simulation of 3D columnar dendrite growth in a 1 mm^3 domain with around 36 billion grid points and 4000 initial seeds.

5.5 Large scale columnar growth under forced convection

Columnar dendrite growth was also simulated in presence of forced convection. At the beginning, arrays of seeds with crystallographic orientations all perpendicular to the bottom face were placed in the domain. This is to better show the effect of fluid flow on the dendrite morphologies. A uniform flow of 7 mm/s velocity enters from the left side, perpendicular to the growth direction. The melt convection washes the solute from the interface in the left face of the dendrites and accelerates the growth in that direction. Similar to what was discussed in the previous chapter, the dendrite arms grow faster in the upstream direction. Interestingly, even the secondary arms perpendicular to the flow direction grow faster, when convection is present.

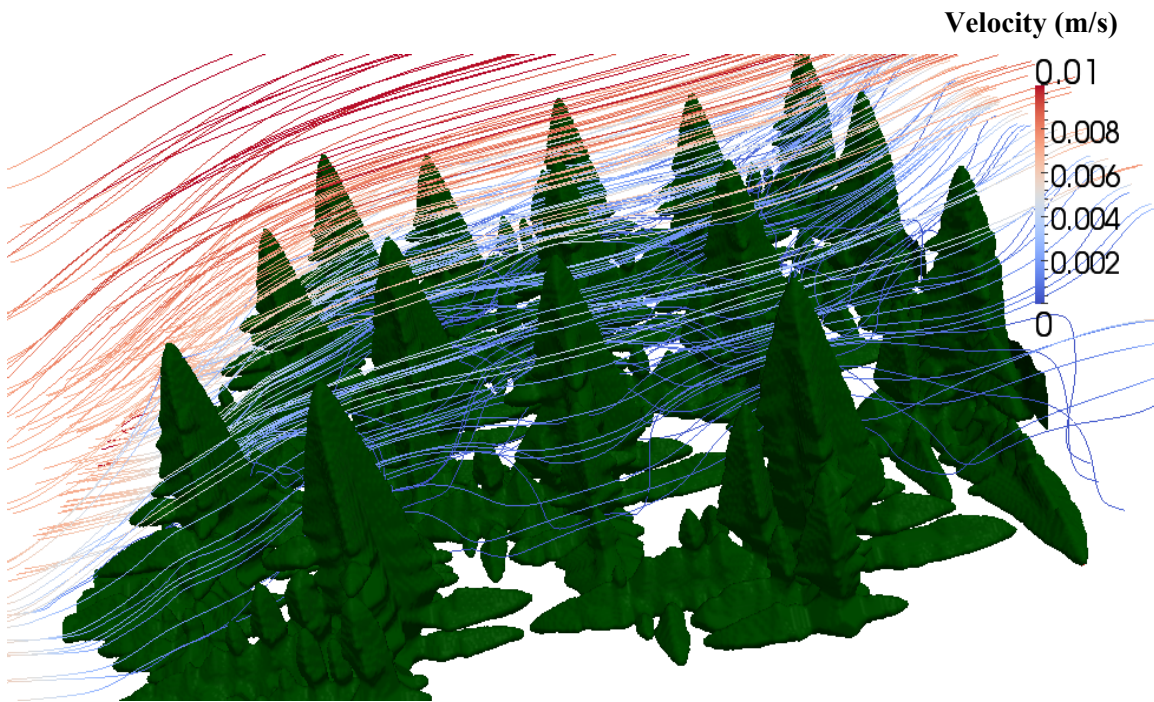


Figure 5.7 3D columnar dendrites growing in an undercooled melt of Al-3wt%Cu. The domain contains around 173 million 3D lattice points that corresponds to a $180 \times 180 \times 144 \text{ } (\mu\text{m})^3$ physical domain.

5.6 Conclusions

A parallel LB-CA model was developed for simulating dendritic solidification in 3D. The model successfully captures the morphology of dendritic microstructure and solute distribution in three dimensions. Exploiting the local characteristics of both LB and CA methods, the presented model enables large scale simulations in macroscopic size domains. The model exhibited a good computational efficiency and parallel scalability. An excellent speed-up performance to thousands of computing cores across the nodes of a computer cluster was demonstrated, along with a near-perfect scale-up performance. Large domain simulations with and without convection were discussed. The special characteristics offered by the presented model, makes it a great tool for simulating large domain solidification problems with good computational efficiency and parallel scalability.

The results of this chapter are partially presented in the proceedings of the 2013 TMS Annual Meeting [5, 6] and the 8th Pacific Rim International Conference on Advanced Materials and Processing [7]. In addition, a manuscript is under preparation based on the results presented in this chapter, to be submitted for journal publication.

5.7 References

- [1] W. L. George, J. A. Warren, A parallel 3D dendritic growth simulator using the phase-field method, *Journal of Computational Physics* 177 (2002) 264–283.
- [2] Z. Guo, J. Mi, P. S. Grant, An implicit parallel multigrid computing scheme to solve coupled thermal-solute phase-field equations for dendrite evolution, *Journal of Computational Physics* 231 (2012) 1781–1796.
- [3] T. Shimokawabe, T. Aoki, T. Takaki, T. Endo, A. Yamanaka, N. Maruyama, A. Nukada, S. Matsuoka, Peta-scale phase-field simulation for dendritic solidification on the TSUBAME 2.0 supercomputer, 2011 International Conference for High Performance Computing, Networking, Storage and Analysis, SC '11, ACM, New York, NY (2011) 3:1–3:11.
- [4] The HDF Group., Hierarchical data format version 5, <http://www.hdfgroup.org/HDF5> (2012).
- [5] M. Eshraghi, B. Jelinek, S. D. Felicelli, A three-dimensional lattice Boltzmann-cellular automaton model for dendritic solidification under convection, 2013 TMS Annual Meeting & Exhibition, San Antonio, TX (2013).
- [6] B. Jelinek, M. Eshraghi, S. D. Felicelli, Large scale parallel lattice Boltzmann model of dendritic growth, 2013 TMS Annual Meeting & Exhibition, San Antonio, TX (2013).
- [7] S. D. Felicelli, M. Eshraghi, B. Jelinek, Large-scale simulation of dendritic solidification, The 8th Pacific Rim International Conference on Advanced Materials and Processing, Waikoloa, HI (2013).

CHAPTER VI

SUMMARY AND FUTURE WORKS

6.1 Summary

In summary, this dissertation described the numerical models based on LB and CA methods for modeling phase change and dendritic solidification.

Development of a new LB model for solving heat conduction problems with phase change was discussed. Despite the previous explicit schemes, the model uses an implicit algorithm to deal with the latent heat source term of the energy equation. Several validation cases were presented, demonstrating the capabilities of the model. In addition, results showed that the proposed LB model outperforms FE models in computational efficiency. The model offers a great potential for solving heat and mass transfer problems incorporating phase transformations.

Understanding the kinetics of dendritic solidification is very crucial in order to design materials with enhanced properties. A three dimensional LB-CA model was introduced for simulating solute-driven dendrite growth. The model successfully captured the morphology of dendritic microstructure in three dimensions. Comparing the growth features over a range of undercoolings showed a good agreement between the simulation results and the theoretical predictions. Effect of the anisotropy of surface energy on the dendritic morphologies was studied. When larger anisotropy parameters were selected, a branchless dendrite with sharp edges grew with high tip velocity. On the other hand,

when smaller anisotropy parameters were used, a dendrite with well-developed branches and low tip velocity was produced.

Furthermore, kinetics of dendrite growth under forced melt convection was studied using a three-dimensional LB model. The results showed that growth kinetics and dendritic morphology are significantly affected by the presence of fluid flow. The primary and secondary arms grew faster in the upstream direction, and significantly slower in the downstream direction. The fluid flow did not show a noticeable impact on the transverse arms and the tip velocity in those directions was similar to the case without convection. A comparison with 2D results revealed that 3D dendrites grow faster in general, but the difference between the velocity of upstream and downstream arms was more significant in 2D simulations. Moreover, 3D dendrites seemed to be more likely to form side branches. It was found that the center of the 3D dendrite was slightly displaced upstream under the influence of melt convection. The displacement increased with inlet velocity. Increasing the degree of undercooling accelerated the growth rate in all directions. By increasing the magnitude of flow velocity, the convection effects were intensified. The influence on the downstream arm seemed more significant in comparison with the upstream arm. The growth rate slowed down in all branches when the alloy contained a higher solute concentration. The size ratio of the upstream arm to the downstream arm grew by increasing inlet velocity and solute content, and decreasing undercooling.

Exploiting the local characteristics of both LB and CA methods, the model was parallelized using MPI technique with spatial domain decomposition. Large scale simulation of dendritic solidification in macroscopic domains of 1 mm^3 size were

presented, which is the largest dendrite growth simulation to the date. In addition, growth of columnar dendrites under melt convection was discussed. The parallel efficiency of the model was also assessed. The model showed a very good speed up performance on up to thousands of processors and an almost perfect scale up performance.

Considering the special capabilities of the model, e.g. simple implementation, computational efficiency, and excellent parallel performance, it can be employed as a great tool for simulating solidification phenomena in 3D macroscopic domains.

6.2 Awards and recognition

The achievements of this dissertation were recognized by several awards. In 2011, I was awarded the NSF fellowship to attend the European-US Summer School on High Performance Computing Challenges in Computational Sciences. I was one of 35 people who were selected from more than 140 US applicants. The goal of the program, which covers all expenses for a one-week training course at Lake Tahoe, CA, was to expand the knowledge of the attendees in high performance computing and its applications in multiple fields of science and engineering. I was also selected to receive the NSF Summer Institute Fellowship to attend the Materials Genome Short Course in 2013. In addition, I received support from the Bagley College of Engineering (BCoE) through a BCoE Graduate Fellowship for the 2011-2012 and 2012-2013 academic years. Recently, I was selected as the 2013 Outstanding Graduate Student Researcher for the Bagley College of Engineering. I was also selected by the Graduate School to receive Travel Assistant Grant for Graduate Students (TAGGS) award to present my work at the 8th Pacific Rim International Conference on Advanced Materials and Processing.

The research presented in this dissertation was reflected in the public reports as well. The dendrite growth modeling was featured in the 2011-2012 Annual Report of the Center for Advanced Vehicular Systems [1]. Moreover, the work on dendritic solidification also made the cover and was featured in the 2012 Research Windows Magazine, Mississippi State University [2].

In order to provide computational resources for this research, a proposal was submitted to the Extreme Science and Engineering Discovery Environment (XSEDE) [3]. XSEDE is a powerful and robust collection of advanced computing resources that is funded by National Science Foundation and shares computing resources, and data with the researchers. The proposal, “Large scale modeling of microstructural evolution during alloy solidification”, was awarded a Research Allocation by XSEDE in 2012. Through this research allocation, we received 500,000 CPU-hours on Gordon at the San Diego Supercomputer Center, 150,000 CPU-hours on Kraken at the National Institute for Computational Sciences, 10,000 CPU-hours on Nautilus at the National Institute for Computational Sciences for visualization, and 5 storage units on Albedo at the Pittsburgh Supercomputing Center.

6.3 Future works

6.3.1 Employ the presented model to simulate various casting and solidification processes

The developed model can be adapted with minimum effort to study solidification in many casting processes. By proper adjustment of the boundary conditions and geometric features, the solidification model can be particularized to different casting, welding, and deposition processes which share similar solidification phenomena. The

direct numerical simulation of the dendritic network will provide a relation between macroscopically observable variables like cooling rate or temperature gradient and difficult-to-measure dynamic microscopic features like solute redistribution, and dendrite arm spacing. Although much observation has been done in pictures of static microstructures at different stages of solidification, it has never been possible to capture the dynamic response of these features in an evolving mushy zone. In addition to providing information to better understand the process, it helps to assess, validate and improve macroscale mushy zone numerical tools.

6.3.2 Simulation of freckle formation during alloy solidification

The channel-like macrosegregation defects, also known as freckles, are often observed during directional solidification of metallic alloys. The channels form in the mushy zone between the dendritic arms, declining the mechanical properties and causing subsequent rejection of the casting products. Therefore, understanding the mechanism of freckle formation has always been of great importance. Different phenomena including solute diffusion and redistribution, heat transfer, melt convection and kinetics of dendritic growth contribute in development of freckle defects. While most of previous studies have been focused on two dimensional simulations in macroscale, a three dimensional (3D) simulation in microscale can provide a better insight about the kinetics of freckle formation. Given the local-type nature and the good scalability for many processors, the 3D model presented in this work can be used to efficiently simulate the formation of plume-type flow between columnar dendrites, interdendritic segregation and eventual formation of freckles in large 3D domains.

6.3.3 Calculation of the interdendritic permeability

Most of the macroscopic models used for modeling solidification processes consider a porous media to simulate the mushy zone in the solidifying alloys. In such macroscale simulations, permeability is a determining factor that has an important role in accurate simulation of thermo-solutal natural convection and the eventual segregation in the solidified material. There has been a lot of experimental and modeling effort to calculate the permeability in the mushy zone of the solidifying alloys. Most of the numerical models that consider the complicated geometry of dendritic structures in their calculations are focused in 2D. However, it is known that flow regimes are totally different in 3D, which is what happens in reality. The main reason preventing the 3D simulations is the very expensive computational cost that cannot be afforded by the conventional computational fluid dynamics methods. Considering the computational advantages offered by the LB method, the model presented in this dissertation can be used to calculate the permeability of dendritic structures using 3D microscale simulations. The model can be considered as a great tool for calculation of permeability in various metallic alloys in different conditions that can be further used for macroscopic simulation of casting and solidification processes.

6.3.4 A pure lattice Boltzmann model for dendrite growth

When complex boundary conditions or high cooling rates are applied, the CA model used in this work may suffer from mesh-induced anisotropy problems leading to artificial effects in the simulation results. The implicit scheme described in Chapter II can be used to develop a pure LB model for dendritic solidification. The model is expected to be more accurate without having the anisotropy problems of the CA algorithm, even

when a larger mesh size is employed. The model can be used to simulate dendrite growth under large temperature gradients and severe cooling conditions with more accuracy.

6.3.5 A multi-grid lattice Boltzmann model with superior computational performance

In order to improve the efficiency of the model, especially when fluid flow is included, a multiple grid LB model can be developed. Different lattice spacing is used for each transported quantity, determined by time step and relaxation time. Embedded-type grids facilitate the transfer of information between lattices. The multiple grid scheme ensures stability and convergence while allowing larger time steps. Considering the fact that LB simulations are very memory-demanding, especially in 3D, this scheme can significantly reduce the memory requirements. In addition, by reducing the number of mesh points, the cost of communications for parallel processing purposes decreases considerably.

6.4 References

- [1] Transport phenomena research has the right moves, Annual Report 2011-12, Center for Advance Vehicular Systems, Mississippi State University (2012) 12-13.
- [2] Scientists see microstructures in a new way, Research Windows, Mississippi State University (2012) 6-9.
- [3] The Extreme Science and Engineering Discovery Environment (XSEDE), <https://www.xsede.org/>.